An experimental investigation of the effects of compressibility on a turbulent reacting mixing layer

By M. F. MILLER†, C. T. BOWMAN AND M. G. MUNGAL

Mechanical Engineering Department, Stanford University, Stanford, CA 94305, USA

Experiments were conducted to investigate the effect of compressibility on turbulent reacting mixing layers with moderate heat release. Side- and plan-view visualizations of the reacting mixing layers, which were formed between a high-speed high-temperature vitiated-air stream and a low-speed ambient-temperature hydrogen stream, were obtained using a combined OH/acetone planar laser-induced fluorescence imaging technique. The instantaneous images of OH provide two-dimensional maps of the regions of combustion, and similar images of acetone, which was seeded into the fuel stream, provide maps of the regions of unburned fuel. Two low-compressibility ($M_c = 0.32, 0.35$) reacting mixing layers with differing density ratios and one high-compressibility ($M_c = 0.70$) reacting mixing layer were studied. Higher average acetone signals were measured in the compressible mixing layer than in its low-compressibility counterpart (i.e. same density ratio), indicating a lower entrainment ratio. Additionally, the compressible mixing layer had slightly wider regions of OH and 50% higher OH signals, which was an unexpected result since lowering the entrainment ratio had the opposite effect at low compressibilities. The large-scale structural changes induced by compressibility are believed to be primarily responsible for the difference in the behaviour of the high- and low-compressibility reacting mixing layers. It is proposed that the coexistence of broad regions of OH and high acetone signals is a manifestation of a more biased distribution of mixture compositions in the compressible mixing layer. Other mechanisms through which compressibility can affect the combustion are discussed.

1. Introduction

Interest in the development of high-speed propulsion systems (e.g. SCRAMJETs) has led to considerable research on compressible turbulent shear flows with the objective of understanding the fundamental mechanisms through which compressibility affects mixing and combustion. The plane mixing layer has been the focus of much of this research since it is one of the simplest free shear flows. Additionally, a large body of data exists on incompressible mixing layers, providing a well-established baseline with which to compare.

Much of our current understanding of the effects of compressibility on free shear flows is based upon the results of experimental and computational studies of non-reacting two-stream mixing layers. Bogdanoff (1983) and Papamoschou & Roshko (1988) introduced the concept of the convective Mach number as a scaling parameter

† Present address: Physical Sciences Inc., 20 New England Business Center, Andover, MA 01810, USA.

for compressibility effects in mixing layers, and throughout this paper, the definition of the convective Mach number, M_c, derived by Papamoschou & Roshko for equal free-stream specific heat ratios, $\gamma_1 = \gamma_2$, will be adopted:

$$M_c \equiv \frac{U_1 - U_2}{a_1 + a_2},$$

where U_1 and U_2 are the velocities of the high- and low-speed streams, respectively, and a_1 and a_2 are the corresponding free-stream sound speeds. As was demonstrated by these investigators, the effect of compressibility on the mixing layer growth rate can be isolated from the effects of the free-stream velocity ratio, $r \equiv U_2/U_1$, and density ratio, $s \equiv \rho_2/\rho_1$, by normalizing the compressible mixing layer growth rate by the growth rate of an incompressible mixing layer with the same velocity and density ratios. When this is done, the growth rate data plotted versus M_c collapse onto a single curve. For $M_c > 0.4$, the growth rate decreases with increasing M_c, and as will be seen, other mixing layer properties display a similar behaviour with convective Mach number. In the present discussion, we will restrict our attention to mixing layers with convective Mach numbers less than unity.

An alternative measure of compressibility is the gradient Mach number concept introduced by Sarkar (1995), which correctly predicts the scaling of compressibility with free-stream conditions in both shear flows and boundary layers. For the mixing layer, the gradient and convective Mach numbers are essentially equivalent, with the gradient Mach number being about a factor of two higher than the convective Mach number, so that in this paper the convective Mach number will be used for consistency with the work of past investigators.

The decrease in the growth rate with increasing convective Mach number is also predicted by linear stability analyses and direct numerical simulations, which show that the two-dimensional Kelvin–Helmholtz instability mode becomes less amplified with increasing compressibility and, as a result, the obliquely oriented instability modes become more significant (e.g. Ragab & Wu 1989; Jackson & Grosch 1989; Sandham & Reynolds 1991). These results suggest that compressible mixing layers have a more three-dimensional structure than incompressible mixing layers, a trend confirmed experimentally by planar laser visualizations of compressible mixing layers (Clemens & Mungal 1992, 1995; Elliott, Samimy & Arnette 1992; Messersmith, Dutton & Krier 1991; Bonnet, Debisschop & Chambres 1993). The two-dimensional spanwise-oriented vortical structures characteristic of incompressible mixing layers are observed in the low-compressibility mixing layers, while the structure of the compressible mixing layer is more three-dimensional and more disorganized. Clemens & Mungal (1995) showed that these structural changes occur gradually with increasing compressibility; however, in general, the mixing layer structure resembles the incompressible mixing layer structure for $M_c < 0.4$, but is quite three-dimensional for $M_c > 0.6$.

The probability of finding molecularly mixed fluid in the mixing layer (mixing efficiency) appears to be relatively insensitive to changes in compressibility. For an increase in the convective Mach number from 0.28 to 0.62, Clemens & Mungal (1995) reported an increase of approximately 20 % in the molecularly mixed fluid probability, although this conclusion was based on passive scalar measurements which were not fully resolved spatially. Dutton *et al.* (1990) reported a similar trend using Mie scattering measurements from seeded particles. Clemens & Paul (1995) devised a technique for measuring mixing efficiency which is insensitive to the effects of spatial resolution based on oxygen quenching of nitric oxide fluorescence. Applying this technique to an axisymmetric shear layer, they measured probabilities of 45 % and

48% at $M_c = 0.35$ and 0.82, respectively, which are very close to those measured in incompressible mixing layers at similar Reynolds numbers (e.g. Mungal & Dimotakis 1984). Using this same measurement strategy, Island (1997) found no apparent dependency of the mixing efficiency on convective Mach number in planar mixing layers. Hall, Dimotakis & Rosemann (1991), who used a fast chemical reaction technique to measure molecular mixing, reported a significant decrease in the mixing efficiency at higher compressibilities; however, subsequent measurements in the same facility support the conclusion that compressibility has only a weak effect on molecular mixing (Dimotakis & Leonard 1994).

Based on measurements of the mean composition of the molecularly mixed fluid in a compressible mixing layer ($M_c = 0.96$), Hall *et al.* (1991) inferred a volumetric entrainment ratio of $E_v \equiv V_1/V_2 \approx 1$. For the experimental free-stream conditions, the incompressible mixing layer correlation of Dimotakis (1986) predicts $E_v = 4.5$; thus, the compressible mixing layer entrainment ratio appears to be substantially different from that of its incompressible counterpart. Since Dimotakis relied on arguments based on the two-dimensional nature of the large-scale structure of incompressible mixing layers to derive the dependence of the entrainment ratio on the free-stream speed and density ratios, it is plausible that the structural changes induced by compressibility (2D→3D) are responsible for the change in the mean molecularly mixed fluid composition.

Despite recent and past interest in supersonic combustion, few compressible reacting shear flows (i.e. $M_c > 0.6$) have been studied experimentally. In past investigations, a common configuration was the sonic injection of ambient-temperature hydrogen into supersonic high-temperature air. Several of these experiments used configurations similar to that of a mixing layer with the hydrogen injected parallel to the supersonic air flow (Burrows & Kurkov 1973; Cohen & Guile 1969; Cheng *et al.* 1994); however, the convective Mach numbers of these flows were generally low ($M_c < 0.4$). Erdos *et al.* (1992) investigated high-compressibility reacting mixing layers ($M_c = 0.86, 2.5$), but reported only measurements of wall static pressure and surface heat flux. Barlow *et al.* (1992) studied an annular reacting mixing layer in the near field of a supersonic jet of air mixing with a coflow composed of the combustion products from a fuel-rich premixed hydrogen–air flame. Comparisons of OH planar laser-induced fluorescence (PLIF) visualizations of the mixing layer at $M_c = 0.1$ and $M_c = 0.4$ indicated a lower degree of organization with increasing compressibility, although some of the observed differences may have been due to the increased Reynolds number of the higher compressibility case.

The studies of mixing and entrainment in mixing layers discussed above suggest several mechanisms through which compressibility can affect mixing and combustion. Most notably, the transition of the large-scale structure from periodic and primarily two-dimensional, to more disorganized and three-dimensional, with increasing compressibility may affect how fluid is entrained into the mixing layer. The observation of Hall *et al.* (1991) that the entrainment ratio of a compressible mixing layer is different from that of its incompressible counterpart may be a manifestation of these structural changes. In the case of combustion, a change in entrainment ratio would affect the overall stoichiometry of the mixing layer, which could alter its heat release and flame holding characteristics.

The objective of the present work is to investigate the effect of compressibility on combustion in a two-stream mixing layer, focusing on the role played by the large-scale structural changes induced by compressibility. Figure 1 is a schematic of the reacting mixing layer configuration studied, which consists of a high-speed high-temperature
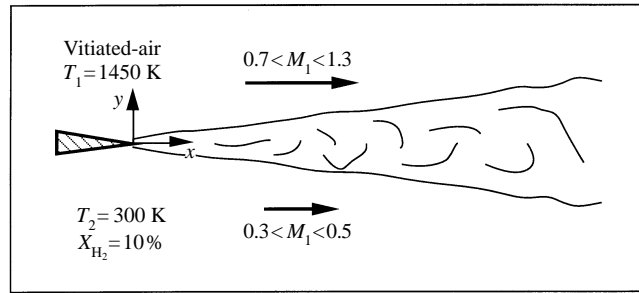
FIGURE 1. Nominal free-stream conditions of the reacting mixing layers.

oxidizing stream and a low-speed ambient-temperature fuel stream. The free-stream static temperatures and compositions were chosen to obtain spontaneous ignition in the mixing layer. The mixing layer compressibility was varied by adjusting either the high-speed-stream Mach number or the molecular weight, and therefore the sound speed, of the fuel stream diluent. Since changes in the entrainment ratio may be one mechanism through which large-scale structural changes affect the combustion, the experiments were designed to investigate the role of the entrainment ratio as well. The entrainment ratio of incompressible mixing layers is sensitive to the free-stream density ratio (Konrad 1976; Dimotakis 1986; Frieler & Dimotakis 1988); thus, by varying the density ratio of the mixing layer at low compressibilities, the effect of the entrainment ratio on combustion was investigated in the absence of compressibility effects. The density ratio was varied by changing the molecular weight of the fuel stream diluent. Visualizations of the mixing layer obtained using a combined OH/acetone PLIF imaging technique are the primary means by which the reacting mixing layer cases are compared.

The remainder of the paper is organized as follows. Section 2 describes the experimental apparatus. Section 3 documents the experimental conditions of the reacting mixing layers studied and discusses the basis of their comparison. Section 4 discusses the interpretation of the OH and acetone fluorescence signals in the context of the reacting mixing layers. Section 5 presents the experimental results, which are discussed in §6. Conclusions are given in §7. Complete details of this work are contained in Miller (1994).

2. Experimental apparatus

2.1. *Flow facility*

The flow facility, which is shown schematically in figure 2, is a large-scale blowdown type consisting of four main components: vitiated-air-stream supply system, fuel-stream supply system, mixing layer facility (wind tunnel) and exhaust system. A vitiation heater burning hydrogen and oxygen-enriched air under fuel-lean conditions is used to produce the high-temperature air stream (Marquardt Company, Sudden Expansion, (SUE) Burner). The fuel stream is hydrogen diluted with nitrogen or helium. Upon entering the mixing layer facility, each stream is accelerated through a nozzle and is discharged into the test section where ignition occurs spontaneously. After exiting the test section, the hot gases are quenched by water sprays and nitrogen gas dilution in the exhaust system. Components of the facility have been described previously by Clemens (1991) and Clemens & Mungal (1995), who performed non-
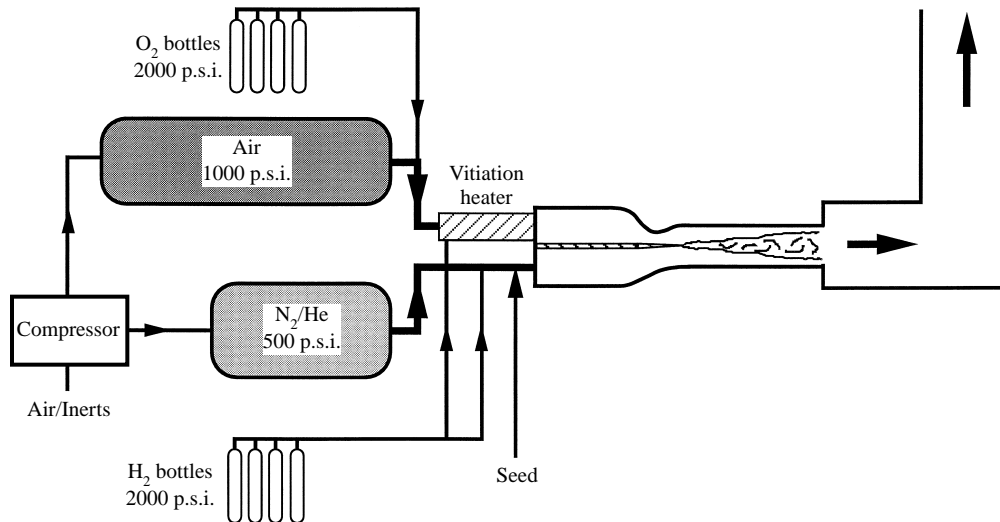
FIGURE 2. Supersonic combustion tunnel flow facility schematic.
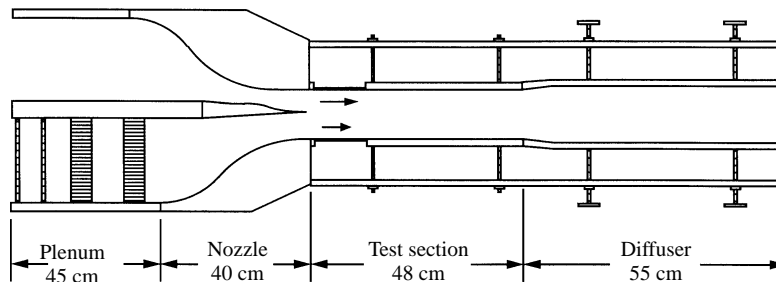
FIGURE 3. Mixing layer facility schematic.

reacting supersonic mixing layer experiments in it; however, major modifications to the facility were required for the execution of the reacting flow experiments, which are detailed in Miller *et al.* (1993, 1994) and Miller (1994).

Five independently controlled gas flows are required to produce the two streams of the reacting mixing layer. Three input gas flows to the SUE burner – air, oxygen and hydrogen – are required to produce the vitiated-air stream, while the fuel stream requires two flows: diluent (nitrogen or helium) and hydrogen. The SUE burner air flow is supplied by a 5 m³, 67 atm pressure vessel which is charged by a compressor capable of delivering breathing quality air (filtered and dried). The fuel stream diluent flow is supplied by a 2.5 m³, 37 atm pressure vessel which was charged with nitrogen from a cryogenic storage system or helium from high-pressure gas cylinders. The oxygen and hydrogen flows are supplied by multiple high-pressure gas cylinders manifolded together. All five of the primary gas flows are metered through choked venturis using a globe-style control valve to regulate the upstream total pressure.

The mixing layer facility, which is shown schematically in figure 3, is approximately 2 m long and has a rectangular cross-section with a constant width of 10 cm. To withstand the heat transfer loads associated with the high-temperature flow, the facility is constructed primarily of water-cooled copper components. By preheating the facility

to approximately 80 °C prior to each experiment, condensation of the water vapour in the vitiated-air flow was prevented. While the fuel stream passes through a series of flow-conditioning elements in the lower plenum to ensure good flow quality, the high temperature of the vitiated-air stream prevented the use of flow-conditioning devices in the upper plenum. The lower contraction has an area ratio of 2.3:1 with an exit height of 5.5 cm. The upper contraction has an area ratio (based on throat area) of 5.5:1. The supersonic nozzle, the contour of which is machined into the upper surface of the splitter tip, had a design Mach number of 1.23 with an exit height of 2.5 cm. The same splitter tip was used for the supersonic and subsonic vitiated-air-stream experiments; thus, for the subsonic condition, the flow experiences a deceleration from the throat to the exit plane of the nozzle. The expansion is slight, however, and the resulting pressure gradient does not significantly affect the flow.

The test section measures 45 cm long, 8 cm high (at the entrance plane) and 10 cm wide. The test section upper and lower walls are adjustable so that the streamwise pressure gradient can be minimized. Optical access is provided by 1.3 cm thick uncooled quartz windows which allow the upstream or downstream two-thirds of the test section length to be viewed at one time. All of the windows are mounted such that their interior surfaces were flush with the test section walls to within 0.08 mm.

The facility is operated remotely using two IBM AT computers. A reacting flow experiment consisted of a sequence of five events: initialize systems, ignite SUE burner, ramp flows to their setpoints, steady-state and shutdown. The entire sequence of events lasts less than 40 s, and the duration of the steady-state flow period is approximately 10 s. Absolute pressure transducers are used to measure the venturi total pressures of the primary gas flows and the mixing layer facility plenum pressures, and a 16 channel pressure scanner is used to measure wall static pressures along the length of the test section. A thermocouple is used to measure the burner outlet temperature. Also, the walls of the facility are instrumented with thermocouples to verify adequate cooling of all critical components.

2.2. *Imaging techniques*

Several techniques were used to visualize the reacting mixing layers: schlieren visualizations were used to determine the mixing layer growth rates and to verify the quality of the test section flow conditions, ultraviolet (UV) emission images were used to determine the mean location of the reaction zone, and the combined OH/acetone PLIF imaging technique was used to visualize the instantaneous structure of the reacting mixing layer.

The schlieren visualizations were obtained using a folded Toepler schlieren system consisting of a 20 ns spark gap lamp (Xenon Corp.), two 30.5 cm parabolic ($f/6$) mirrors, two 30 cm by 10 cm flat mirrors, a razor blade knife edge, and a CCD video camera (Pulnix TM540) equipped with a telephoto lens. The images were acquired using an IBM AT computer equipped with a frame grabber board (Data Translation 2851).

The primary elements of the combined OH/acetone PLIF imaging system are shown in figure 4. A single 8 ns, 20 mJ pulse from a frequency-doubled Nd:YAG-pumped dye laser (Lumonics models YM-1200, HD-500, HT-1000) was formed into a collimated sheet using three cylindrical lenses. The first two lenses, -50 mm and 500 mm focal lengths, form a cylindrical telescope which spread the beam into a collimated 9 cm tall sheet. The final lens, 500 mm focal length, focused the sheet to a 500 μm waist. The same arrangement of sheet-forming optics was used for both the side and plan views. The laser was tuned to the $P_1(7)$ transition of the (1,0) band of the $A^2\Pi^+$-$X^2\Sigma$ system of OH at 285 nm, and the laser linewidth was approximately 0.5 cm^{-1}. Each
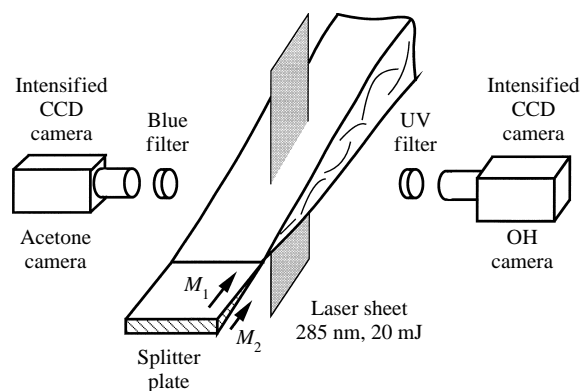
FIGURE 4. Combined OH/acetone PLIF imaging system schematic.

fluorescence signal was recorded on a separate intensified and cooled CCD camera (Princeton Instruments, ICCD 576/RB) with an intensifier gate width of 400 ns. The CCD array is 578 by 384 pixels, but on-chip 2 by 2 binning of pixels was used to increase the framing rate of the system to approximately 5 Hz. The OH camera was equipped with Schott WG305 and UG11 filters and a 105 mm, $f/4.5$ UV Nikkor lens. The acetone camera was equipped with a 500 nm low-pass filter (Andover 500FL0750) and a 50 mm, $f/1.2$ standard glass (UV blocking) Pentax lens. Each camera was interfaced to an IBM AT computer which was used to program the camera and acquire the images. The fields of view of the OH and acetone cameras were aligned to within a pixel over most of the imaged region to reduce the amount of post-processing of the images.

The method used to seed acetone into the fuel stream was patterned after that used by Clemens (1991) for injecting alcohol into the main flows for planar laser Mie scattering experiments. Ten metres upstream of the entrance to the low-speed plenum, liquid acetone is sprayed directly into the fuel stream flow through a fine atomizing nozzle. The resulting acetone droplets, which have diameters less than 100 μm, evaporate prior to reaching the test section.

The time-averaged UV emission from the reacting mixing layers was imaged using a camera system identical to that used to record the OH PLIF, except that intensifier gate widths of between 10 and 45 ms were used and no binning of pixels was performed.

3. Overview of experimental conditions

The experimental conditions of the three reacting mixing layers studied are listed in table 1. Since the OH/acetone PLIF images are the primary means by which the mixing layers are compared, the primary focus of this discussion is on the mixing layer conditions at the position in the test section where these images were obtained. For the purposes of discussion, the three cases will be referred to as denoted in the table headings: Fast/N_2, Fast/He and Slow/N_2, where Fast and Slow denote the vitiated-air Mach numbers $M_1 = 1.23$ and 0.70, respectively, and He and N_2 denote the fuel stream diluents, helium and nitrogen, respectively. The dynamical parameters of each reacting mixing layer, based on these free-stream conditions, are listed in table 2.

Case	Fast/N$_2$		Fast/He		Slow/N$_2$	
M_c	0.70		0.35		0.32	
	Vitiated-air stream	Fuel stream	Vitiated-air stream	Fuel stream	Vitiated-air stream	Fuel stream
Total temperature (K)	1790	285	1790	290	1590	280
Mach number	1.23	0.41	1.23	0.35	0.70	0.53
Static temperature (K)	1460	276	1460	279	1490	265
Velocity (m s^{-1})	950	150	950	350	550	185
Molar composition						
O$_2$ (%)	23	—	23	—	22	—
H$_2$O (%)	25	—	25	—	24	—
N$_2$ (%)	52	90	52	—	54	90
H$_2$ (%)	—	10	—	10	—	10
He (%)	—	—	—	90	—	—
Mass flow rate (kg s^{-1})	0.49	0.87	0.52	0.28	0.28	1.2
Static pressure (atm)	0.94		0.97		0.92	

TABLE 1. Reacting mixing layer free-stream conditions

Case	Fast/N$_2$	Fast/He	Slow/N$_2$
M_c	0.70	0.35	0.32
$s = \rho_2/\rho_1$	5.1	0.75	5.4
$r = U_2/U_1$	0.15	0.37	0.34
$(E_v)_i$	3.8	1.1	3.3
$(\delta)_{x=22\,\mathrm{cm}}$(cm)	3.7	2.5	3.1
$(Re_\delta)_{x=22\,\mathrm{cm}}$			
$\Delta U\delta/\nu_1$	110000	56000	42000
$\Delta U\delta/\nu_2$	1900000	125000	710000
$(\delta/(U_1-U_2))_{x=22\,\mathrm{cm}}$(µs)	43	39	89
$(2x/(U_1+U_2))_{x=22\,\mathrm{cm}}$(µs)	400	340	600

TABLE 2. Mixing layer dynamical parameters

3.1. *Free-stream conditions*

To ensure that the overall stoichiometry and chemical kinetic time scales of the reacting mixing layers were similar, the vitiated-air-stream static temperature and oxygen mole fraction and the fuel-stream static temperature and hydrogen mole fraction of each case were nominally the same. The vitiated-air total temperatures listed in table 1 were determined from thermocouple measurements of the SUE burner outlet temperature. The vitiated-air temperatures were not exactly the same for all cases; however, the OH PLIF measurements did not have a large sensitivity to variations in static temperatures over this range. Additionally, time-averaged UV emission measurements were obtained over a range of vitiated-air static temperatures to supplement the combined OH/acetone PLIF measurements.

The Slow/N$_2$ (low-compressibility) mixing layer has a high density ratio ($s \approx 5$) as does the Fast/N$_2$ (high-compressibility) case; thus, these two cases provide a basis for the evaluation of the effects of compressibility on the mixing layer structure and combustion at a fixed free-stream density ratio. The primary motivation for including the Fast/He (low-compressibility) case in these experiments was to investigate the

effect of the relative rates of entrainment of fuel and oxidizer on the combustion at low compressibilities. The 'incompressible' volumetric entrainment ratio, $(E_v)_i \equiv V_1/V_2$, for each of the reacting mixing layers, as calculated from the correlation of Dimotakis (1986), is listed in table 2. It is important to keep in mind that there is a distinction between the ratio of the fluxes of free-stream fluid into the mixing layer and the mean composition of the molecularly mixed fluid in the mixing layer (for a discussion see Konrad 1976). Here, and throughout the remainder of this paper, the term entrainment ratio, which will be denoted as E_v, refers to the latter of these definitions.

Owing to experimental constraints, it was not possible to maintain the same velocity ratio for all three reacting mixing layers. The Fast/He and the Slow/N$_2$ cases have velocity ratios of 0.37 and 0.34, respectively, which are quite similar; however, the Fast/N$_2$ case has a velocity ratio of 0.15. In the context of the present measurements, this difference is only significant if it affects the entrainment ratio or large-scale structure of an incompressible mixing layer with the same free-stream speed and density ratio as the Fast/N$_2$ case, that is, its incompressible counterpart. In other words, certain assumptions need to be made about how the Fast/N$_2$ case would behave in the absence of compressibility so that observed differences between the three reacting mixing layer cases yields direct information about the effects of compressibility. Although the entrainment ratio formula of Dimotakis (1986) has been tested primarily at $r = 0.38$, the large-scale-structure streamwise spacing, which is the one term in the entrainment ratio formula that does not contain an explicit dependence on velocity or density ratio, has been observed to be fairly constant over a wide range of velocity and density ratios, indicating that the 'incompressible' entrainment ratio assigned to the Fast/N$_2$ case in table 2 is justified. Additionally, changes in the large-scale structure with changing velocity ratio have not been observed in incompressible mixing layers. These results indicate that the lower velocity ratio of the Fast/N$_2$ case should not complicate the interpretation of the results.

The splitter-tip boundary layer momentum thickness Reynolds numbers for the high-speed stream, $Re_\theta = U_1 \theta_1/\nu_1$, were 1960 and 450 for the $M_1 = 1.23$ and 0.70 cases, respectively, as calculated by STAN7, a turbulent boundary layer code developed by Crawford & Kays (1976). The combined OH/acetone PLIF images were acquired 22 cm downstream of the splitter tip, corresponding to $x \approx 1000\theta_1$ which meets the criterion of Bradshaw (1966) for a fully developed mixing layer. The work of Huang & Ho (1990) and Karasso & Mungal (1996) suggests that the number of vortex pairings a mixing layer has experienced is a more appropriate criterion for determining when a fully developed state has been reached (provided the Reynolds number is high enough). Using a pairing parameter, defined as Rx/λ, where $R = (1-r)/(1+r)$, x is the streamwise distance and λ is the initial instability wavelength, to correlate their measurements, Karasso & Mungal found that a fully developed scalar state is reached after the third vortex pairing, corresponding to $Rx/\lambda \approx 16$–22, with the exact value being somewhat facility dependent. The pairing parameter values for the mixing layers in the present work are $Rx/\lambda = 15$, 16 and 26 ($x = 22$ cm) for the Slow/N$_2$, Fast/He and Fast/N$_2$ cases, respectively. Taken in the context of the above discussion, these values suggest that all of the reacting mixing layers can be considered fully developed. For completeness, a pairing parameter for the compressible mixing layer has been listed, although it is recognized that the concept of a vortex pairing is not well defined for this case.

3.2. *Mixing layer conditions*

The Reynolds numbers listed in table 2 were evaluated using the free-stream velocity difference, the local mixing layer thickness at the OH/acetone PLIF imaging station

and the free-stream viscosities. Since the properties of the vitiated-air and fuel streams differed significantly, two Reynolds numbers are listed for each mixing layer corresponding to the two free-stream viscosities. Based on these Reynolds numbers, the smallest scalar gradients in the flow, which are on the order of $\delta/Re^{3/4}$, were less than 100 μm. Since the spatial resolution of the PLIF imaging system was only about 500 μm, the fluorescence measurements were not fully resolved spatially. This limitation is not of consequence when interpreting the large-scale structure of the mixing layer from the imaging results; however, it is necessary to consider when interpreting the signal levels as indicators of the mixed-fluid composition.

Based on the results of previous non-reacting mixing layer experiments (e.g. Clemens & Mungal 1995), the effects of compressibility on the mixing layer structure at $M_c \approx$ 0.35 (Fast/He and Slow/N_2 cases) will be small, while at $M_c \approx 0.70$ (Fast/N_2 case), the effects will be significant. It is necessary, however, to consider two factors which distinguish the mixing layers in the present work from those in previous studies: heat release and free-stream density ratio. Similarly to incompressible mixing layers with equal-density free streams, the Kelvin–Helmholtz instability mode continues to be the dominant one for unequal-density free streams (e.g. Brown & Roshko 1974; Maslowe & Kelly 1971). The levels of heat release in the reacting mixing layers in this work are within the range investigated by Hermanson & Dimotakis (1989), who found that heat release decreased the mixing layer growth rate but significant changes in the basic large-scale structure were not observed, a result which is consistent with the linear stability analysis of Shin (1992).

Linear stability analyses of compressible mixing layers ($0.6 < M_c < 1$) with unequal-density free streams indicate that, similarly to the equal-density case, the oblique instability modes are as unstable as the two-dimensional instability mode (Sandham 1989; Planche 1992). Planche (1992), who calculated the stability of a reacting mixing layer with free-stream conditions nearly identical to those of the Fast/N_2 case, found that the present level of heat release is not sufficient to significantly affect its stability characteristics so that the structure of the reacting mixing layers will be similar to that observed in non-reacting mixing layers at a similar compressibilities.

Based on the free-stream conditions listed in table 1, the range of expected static temperatures in the reacting mixing layers can be estimated. In figure 5(*a*) the frozen-chemistry and adiabatic-equilibrium mixture temperatures, T_{mix} and T_{eq}, respectively, are plotted as a function of high-speed molar mixture fraction, ξ_n, for the case of nitrogen as the fuel-stream diluent. The high-speed molar mixture fraction is defined as $\xi_n \equiv N_1/(N_1 + N_2)$, where N_i is the number of moles from each free stream ($i = 1$, 2). The frozen-chemistry temperature represents the mixture temperature in the limit of infinitely slow chemistry and shows the effects of pure dilution, while the adiabatic-equilibrium temperature represents the mixture temperature in the limit of infinitely fast chemistry and shows the effects of the maximum heat release. Thus, for a given mixture fraction, the static temperature must lie between the two temperature curves. Also plotted as a function of mixture fraction is the mixture equivalence ratio, $\phi \equiv N_{H_2}/2N_{O_2}$. The plots show that for all mixture fractions, the mixture static temperatures are below the vitiated-air-stream static temperature of 1450 K. For a stoichiometric mixture of the free streams ($\xi_n \approx 0.18$), the temperature rise resulting from complete combustion is about 600 K for the nitrogen cases. For the case of helium as the fuel-stream diluent (not shown), similar trends are observed, although the maximum temperature rise produced by the heat release of combustion is somewhat higher (800 K) due to the lower specific heat of helium.

An important parameter to control when comparing reacting flows is the Damköhler
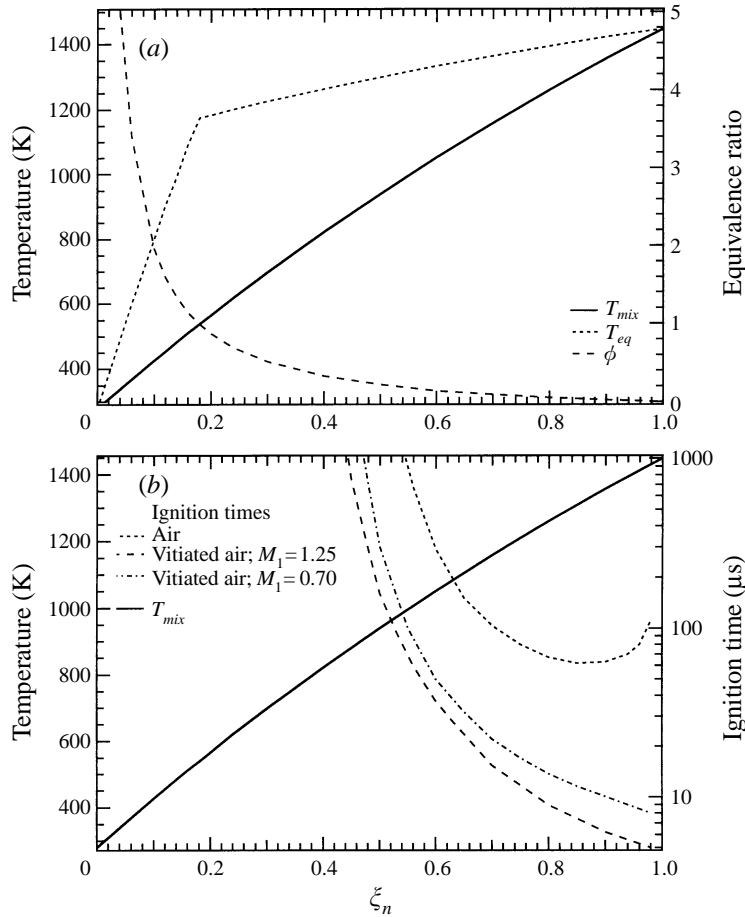
FIGURE 5. Mixing layer conditions as a function of high-speed molar mixture fraction for Fast/N$_2$ and Slow/N$_2$ reacting mixing layers: (*a*) frozen-chemistry, T_{mix}, and adiabatic-equilibrium, T_{eq}, temperatures and equivalence ratio, ϕ; (*b*) T_{mix} and ignition delay times, τ_{ign}, for various vitiated-air-stream conditions.

number, *Da*, which is defined as the ratio of a fluid mechanical or mixing time and a chemical time. High Damköhler numbers indicate fast-chemistry or mixing-limited flows in which the chemical reaction rates are much faster than the mixing rates. Several fluid mechanical time scales which can be used to characterize the mixing process are listed in table 2. The average time to convect from the splitter tip to the OH/acetone PLIF imaging station ($x = 22$ cm) is between 300 and 600 μs. The large-scale eddy turnover time, which is sometimes used as a scaling time for mixing (Broadwell & Breidenthal 1982) and is defined as $\delta/(U_1 - U_2)$, is between 40 and 90 μs at the imaging station. Based on both of these measures, the Slow/N$_2$ case, owing to its lower free-stream velocities, has the longest mixing times – in some cases almost a factor of two longer.

Although the vitiated-air-stream static temperatures are nominally the same for the three mixing layers, their corresponding stagnation temperatures differ because of the differences in their free-stream Mach numbers. An important side effect to consider is that the vitiated-air-stream combustion radical concentrations (e.g. O, H, OH and NO) in the test section differ as well. Since the nozzle expansion process of the vitiated-air

stream is rapid enough that its chemical composition does not stay in equilibrium, the radical concentrations freeze out at a level which depends primarily on their concentrations at the stagnation conditions. Since the higher Mach number cases require a higher total temperature to produce the same static temperature at the expanded condition, the radical concentrations freeze out at a higher level for these cases.

The primary concern over the differences in the vitiated-air-stream radical levels for the Fast and Slow cases is that they may produce differences in the chemical reaction time scales. To investigate this issue, detailed chemical kinetics calculations were performed to investigate the effect of the vitiated-air-stream radical levels on the ignition times of mixtures of the free streams. Although ignition calculations do not include all of the physics necessary to model combustion in these flows, they provide an indication of the sensitivity of the chemical reaction times to the vitiated-air-stream conditions. The mixture ignition times are plotted as a function of ξ_n in figure 5(*b*). For reference, the mixture ignition times in the absence of combustion radicals in the vitiated-air stream (air) are also shown. The ignition times of the Slow case are approximately a factor of two longer than those of the Fast cases, with the longer ignition times being a reflection of the lower radical concentrations in the vitiated-air stream. Since both the mixing and chemical reaction times of the Slow/N_2 case are about a factor of two times longer than those of the other two cases, the resulting overall Damköhler numbers are quite similar, indicating that direct comparisons can be made between the mixing layer cases to evaluate the effects of compressibility on combustion.

4. OH and acetone behaviour in the reacting mixing layers

In addition to using the combined OH/acetone PLIF imaging technique to visualize the instantaneous structure of the reacting mixing layer, the average OH and acetone fluorescence signals will be compared to assess the effect of compressibility and entrainment ratio on the combustion. Thus, it is necessary to discuss the spectroscopic and chemical behaviour of OH and acetone so that the proper interpretation of the fluorescence signals can be established.

4.1. *OH spectroscopy and chemistry*

An analysis of the OH fluorescence measurements (Miller 1994) indicates that only collisional quenching effects are important to consider when comparing the relative OH fluorescence signals of the three reacting mixing layer cases. Limiting our attention to those regions of the mixing layer where significant quantities of OH will be found, that is, where the temperatures are highest ($T > 1000$ K), it was found that the fluorescence signal per unit concentration of OH varies by less than 10 % for the case of helium as the fuel-stream diluent and less than 20 % for the case of nitrogen; thus, interpreting the OH fluorescence signals as an indicator of OH concentration is appropriate. Since the quenching effects will be the same for the Fast/N_2 and Slow/N_2 cases, direct quantitative comparison of the OH signals can be made; however, when comparing these two cases to the Fast/He case, specific heat and quenching differences need to be considered. The quenching analysis indicated that the decreased quenching associated with helium as the fuel-stream diluent leads to about a 25 % increase in OH signal over that of the nitrogen cases.

The ignition envelopes plotted in figure 5(*b*) indicate that OH is likely to be formed in the fuel-lean regions of the mixing layer where the mixture temperatures are the

highest. Since the radical recombination rates have negative temperature dependencies (i.e. the rates increase with decreasing temperature), OH is most likely to survive as a product of the combustion in these regions as well. Although the ignition times cover a wide range of values, a characteristic time scale for OH formation is 5–20 µs ($\xi_n >$ 0.75). Based on the same ignition calculations, the time scale for OH recombination, as it asymptotes to its equilibrium level, is 100–300 µs. Other estimates of the chemical reaction time scales in the mixing layer were obtained from strained laminar diffusion flame calculations using the mixing layer free-stream conditions as the reactant streams (Miller *et al.* 1989). The primary result of these calculations is that for air temperatures above 1200 K the flames did not have a well-defined extinction point. As the strain rate was increased, the product formation decreased significantly; however, because the high-temperature air stream was a constant ignition source, significant radical concentrations continued to be formed in the reaction zone. For example, for a diffusion flame between 1400 K air and 300 K 10% H_2 diluted in nitrogen, conditions similar to those of the reacting mixing layers, the peak water mole fraction in the flame decreased from 10% at a strain rate of 100 s^{-1} to 2% at a strain rate of 30000 s^{-1}. Over the same range of conditions, the peak OH mole fraction remained constant at about 1000 p.p.m. Thus, the formation times for OH in the flame must be less than 30 µs, while the product formation times are considerably longer.

Comparing the OH formation times (10–20 µs) to the local eddy turnover times ($\delta/\varDelta U$) for the reacting mixing layers at the PLIF imaging station (40–90 µs), indicates that the local Damköhler number for OH formation is about 5. Based on the radical recombination and product formation rates estimated from the calculations discussed above, the OH destruction times in the mixing layer are about an order of magnitude slower than the OH formation times, yielding Damköhler number for OH destruction of about 0.5. The results of Masutani & Bowman (1986) and Mungal & Frieler (1988) indicate that the fast-chemistry limit for product formation is reached at $Da \approx 10$, and the slow-chemistry limit is reached at about $Da \approx 1$. Based on these results, the Damköhler number for OH formation is between the fast- and slow-chemistry limits while that for OH destruction is below the slow-chemistry limit; thus, in hotter regions of the mixing layer, OH will survive outside the reaction zones as a product of combustion. For the chemical systems used in the experiments of Mungal & Frieler and Masutani & Bowman, product formation occurs throughout the mixing layer regardless of the local stoichiometry and temperature, which is in contrast to the present work where a minimum temperature is required for the initiation and propagation of the combustion process. Hence, the results of Mungal & Frieler and Masutani & Bowman provide a conservative estimate of the Damköhler number required to reach the fast-chemistry limit – a higher Damköhler number may actually be required in the current experiments.

4.2. *Acetone spectroscopy and chemistry*

For acetone fluorescence to be a reasonable marker of unburned hydrogen in the present reacting mixing layers, several assumptions are necessary. First, acetone must behave chemically similarly to hydrogen. The primary removal mechanism of both acetone (CH_3COCH_3) and hydrogen (H_2) is through radical attack – hydrogen atom abstraction by combustion radicals (H, O and OH). Yip *et al.* (1994) showed that for the conditions of the reacting mixing layers, the radical attack rates of acetone are similar to those of the hydrogen. Miller (1994) has estimated that the radical attack rates are approximately an order of magnitude higher than the pyrolysis rates in the reacting mixing layers; thus, acetone pyrolysis is not a significant removal mechanism

of acetone. Since the molecular weight of acetone is much larger than that of hydrogen, the effects of preferential diffusion on the reactant consumption rates needs to be addressed. As has been discussed previously in the context of the chemistry of OH in the reacting mixing layers, combustion in the mixing layer is not in a fast-chemistry limit so that the majority of the reactant consumption will occur in a 'well-mixed' mode of combustion as opposed to a 'flame-sheet' mode of combustion. Hence, the effects of preferential diffusion on the relative consumption rates of acetone and hydrogen should not be significant.

Secondly, it is also necessary that acetone fluorescence is proportional to acetone concentration. Acetone fluorescence has been shown to be linear with number density at ambient conditions (e.g. Lozano, Yip & Hanson 1992); however, more recently it has been found to have some temperature sensitivity which varies with excitation wavelength (e.g. Tait & Greenhalgh 1992; Wolff *et al.* 1993; Grossman 1993; Grisch, Thurber & Hanson 1995). Grisch *et al.* have compiled the most extensive data set, having measured acetone absorption and fluorescence as a function of temperature ($300 < T < 1000$ K) for a variety of excitation wavelengths ($266 < \lambda < 308$ nm). For the excitation wavelength used in the present experiments, 285 nm, the fluorescence varies by $< 10\%$ for temperatures below 700 K. Above 700 K, the fluorescence decreases with increasing temperature, and by 1000 K the fluorescence is about 30% lower than its 300 K value.

In the context of the present experiments, these results indicate that acetone will perform as a reasonable marker of unburned hydrogen, particularly in the cooler ($T < 1000$ K) fuel-rich regions of the mixing layer where the acetone signals will be highest. In the high-temperature ($T > 1000$ K) regions of the mixing layer, where significant combustion will be occurring and the acetone signals will be low, interpretation of the acetone fluorescence signal will be complicated by the fluorescence temperature dependence. While the acetone will perform quite adequately for the purposes of visualizing the instantaneous structure of the mixing layer (combined OH/acetone PLIF images), quantitative interpretation of the acetone fluorescence signals will need to be done with care.

5. Results

5.1. *Test section static pressures*

The test section static pressure distributions for the three reacting mixing layer cases listed in table 1 are shown in figure 6. The test section pressure was slightly subatmospheric for all cases (0.92–0.97 atm). The pressure matching observed between the two streams is typical for this type of facility (e.g. Clemens & Mungal 1992, 1995; Hall, Dimotakis & Rosemann 1993). For the Fast/N_2 and Fast/He cases, for which the high-speed stream was supersonic, the first static pressure tap reading was consistently low and does not appear to be reliable. Since schlieren visualizations of the mixing layers did not indicate a strong mismatch of pressures for the supersonic cases, this pressure mismatch is not considered to be significant. In general, the streamwise pressure gradient was less than 5% over the length of the test section, with this variation being due to imperfect adjustment of the test section walls. For all cases, the test section top wall was horizontal (0°) while the bottom wall was diverged 1.6° for the Fast/N_2 and Slow/N_2 cases and 0.4° for the Fast/He case.
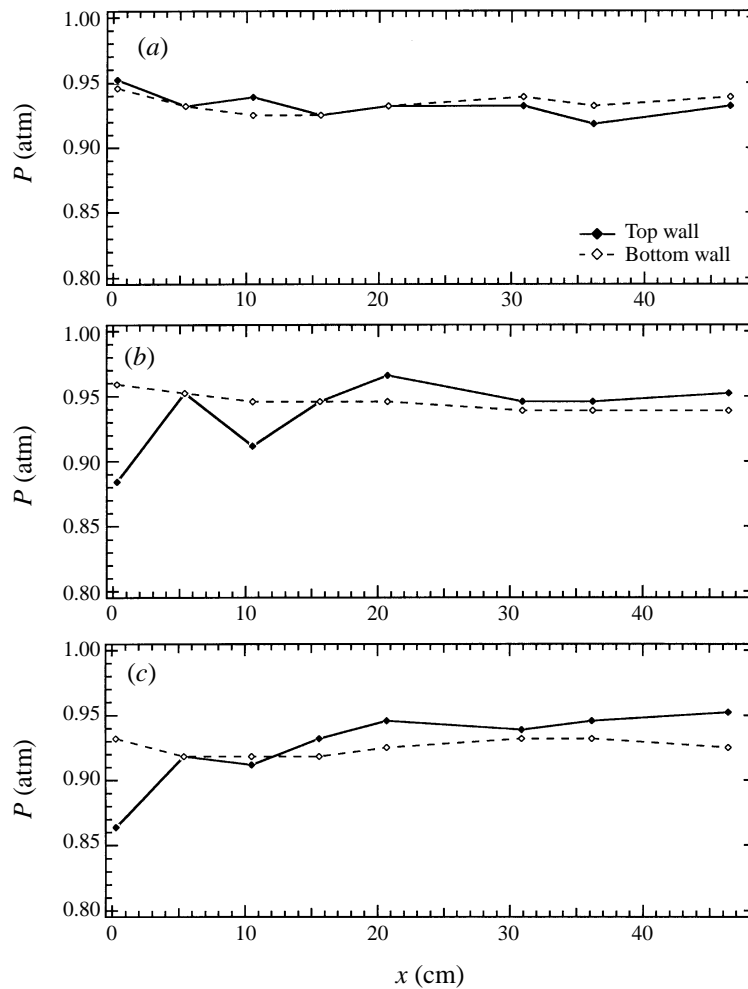
FIGURE 6. Test section static pressure distribution for reacting mixing layers: (*a*) Slow/N_2 (*b*) Fast/He and (*c*) Fast/N_2.

5.2. *Schlieren visualizations*

Representative side-view schlieren visualizations of the Slow/N_2 and Fast/N_2 reacting mixing layers are shown in figure 7. High-quality schlieren images of the Fast/He case were not obtained because the index of refraction difference between the two free streams was too low, causing interferences from thermal gradients in the windows to dominate the images. Each image is a composite of three individual visualizations which are not correlated in time. The knife edge, which was oriented vertically to increase the rejection of interferences, was positioned in the focal plane so that the schlieren was quite sensitive. As a result, little information regarding the mixing layer structure can be discerned.

For the Fast/N_2 case (supersonic vitiated-air stream), a system of weak oblique shock waves is visible in the vitiated-air stream at the entrance to the test section. The wave extending off the top wall is due to a slight mismatch of the test section top wall and the upper contraction (< 0.08 mm). The waves originating from the end of the splitter tip are a shock wave/expansion fan combination which is a result of the flow separating off the splitter tip. Waves are also visible in the fuel stream, emanating from

(a)

(b)
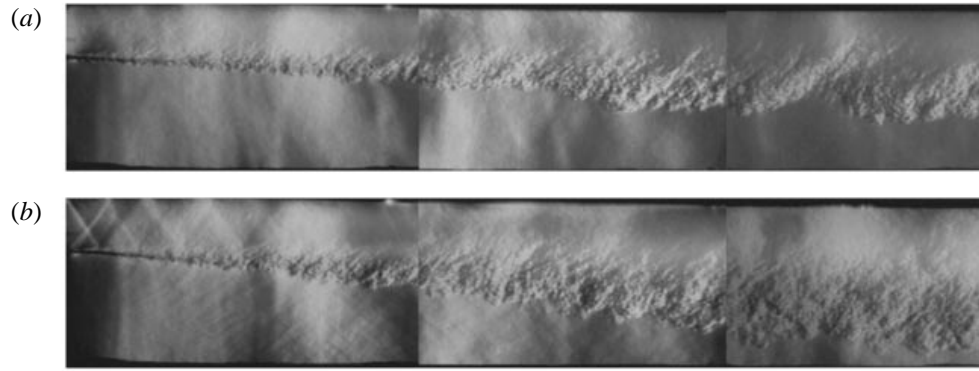
FIGURE 7. Full test section side-view schlieren images of Slow/N_2 (*a*) and Fast/N_2 (*b*) reacting mixing layers. Each image is a composite of three individual images (uncorrelated in time).

Case M_c	x_0(cm)	δ'	δ'/δ_i'
Slow/N_2 0.32	-2.0 ± 0.2	0.13 ± 0.01	0.62 ± 0.06
Fast/He 0.35	N/A	0.11 ± 0.02	0.76 ± 0.11
Fast/N_2 0.70	-3.5 ± 0.5	0.14 ± 0.01	0.40 ± 0.04

TABLE 3. Mixing layer growth rates

the mixing layer and reflecting off the bottom wall of the test section. These waves, which are not seen in the Slow/N_2 visualizations, were observed in both reacting and non-reacting Fast/N_2 mixing layers. Hall *et al.* (1993) observed similar waves in mixing layers under similar conditions and attributed them to disturbances travelling in the mixing layer at a speed which is supersonic relative to the low-speed stream, a conclusion which is consistent with the present results since the Fast/N_2 case is the only case in which the high-speed stream is supersonic relative to the low-speed stream.

For the Slow/N_2 and Fast/N_2 cases, 50 full test section schlieren images were averaged to determine growth rate of the mixing layers. The measured virtual origins, growth rates, and growth rates normalized by those of the incompressible counterparts (i.e. the same *r* and *s*) are listed in table 3. In the absence of schlieren data, the growth rate listed for the Fast/He case was determined by dividing the mixing layer width measured from average OH and acetone PLIF images by the distance to the centre of the imaging station (22 cm). For the other two cases, the mixing layer widths determined from the schlieren and average OH/acetone images were in good agreement. The normalized growth rates, which are also plotted in figure 8, fall within the scatter of non-reacting mixing layer measurements. Since the heat release level in the reacting mixing layers is modest, good agreement with non-reacting mixing layer results is to be expected.

5.3. *UV emission images*

The time-averaged UV emission images of the reacting mixing layers serve primarily two purposes. First, the UV emission images of the region immediately downstream of the splitter tip are used to compare the ignition behaviour of the reacting mixing layers.
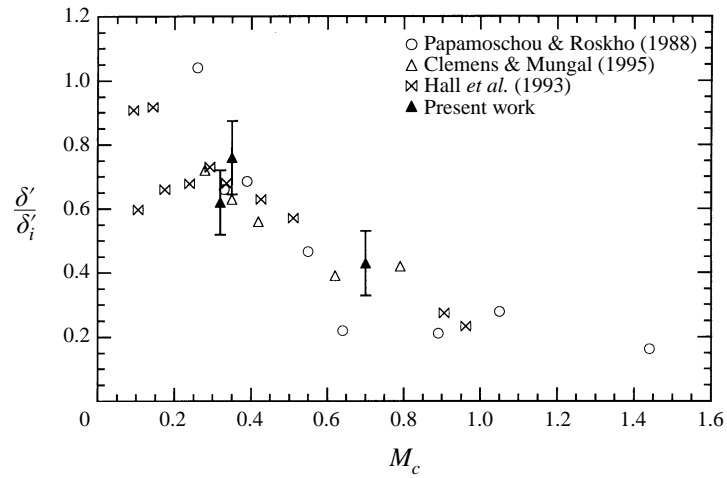
FIGURE 8. Normalized mixing layer growth rate as a function of convective Mach number, M_c.
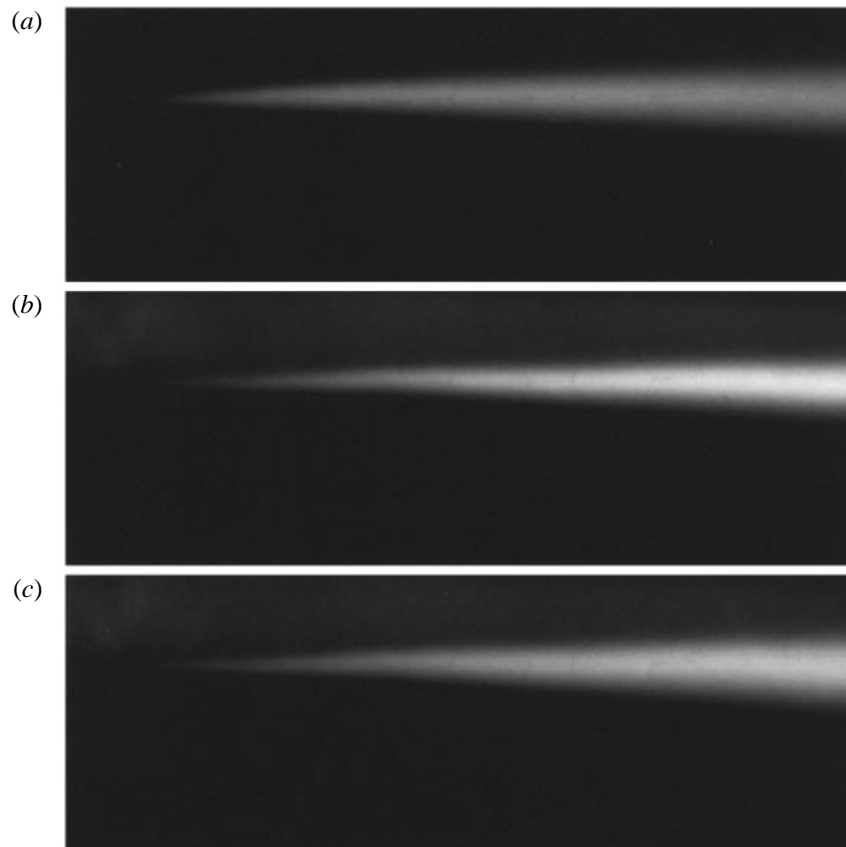
FIGURE 9. Side-view time-averaged UV emission images of the reacting mixing layers at the nominal conditions listed in table 1: Slow/N_2 (*a*), Fast/He (*b*) and Fast/N_2 (*c*).
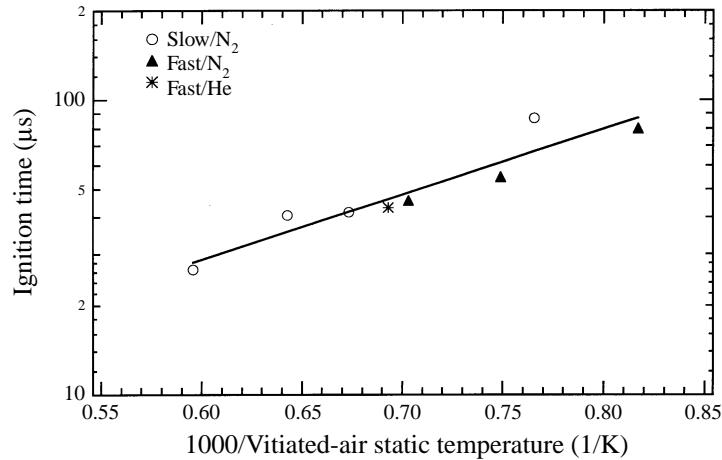
FIGURE 10. Ignition time of the reacting mixing layers as a function of the vitiated-air-stream static temperature. Ignition time determined using extrapolation of maximum slope of UV emission curves.

Second, the UV emission images obtained at the same location as the OH/acetone PLIF images supplement the OH fluorescence measurements as an indicator of combustion intensity. Furthermore, the UV emission images were obtained over a range of vitiated-air static temperatures, allowing a more complete comparison of the reacting mixing layers.

5.3.1. *Ignition behaviour*

Figure 9 shows side-view UV emission images for the three reacting mixing layers cases. The flow is left to right, and the end of the splitter tip is at the left-hand edge of the images. The images are approximately 17 cm wide and 6 cm high. The only correction applied to these images is the subtraction of an average background level. No dramatic differences between the three cases are apparent from the images. The zone of UV emission coincides with a region of the mixing layer adjacent to the vitiated-air stream. The ignition length, defined as the distance from the splitter tip to the point where the maximum slope of the UV emission signal profile extrapolates to the abscissa, is about 2–3 cm for all three cases. Ignition times derived by dividing the ignition lengths by the average velocity of the free streams are compared in figure 10. The times, which vary from 30 to 90 μs over the range of temperatures investigated (1200–1700 K), all fall onto a common line, indicating no major differences in the ignition behaviour of the three reacting mixing layer cases.

Considering the differences in the free-stream conditions of the reacting mixing layer cases (i.e. r, s and M_c) a greater difference in their ignition behaviour might have been expected. Their similarity may be a reflection of the equivalence of the overall Damköhler numbers at each vitiated-air-stream static temperature. One difficulty associated with comparing the ignition behaviour of the reacting mixing layers is that the majority of the ignition process occurs in the development region of the mixing layer so that using ideas based on the far-field behaviour of the mixing layers (e.g. entrainment ratio) to correlate these observations is not appropriate. For example, based on close-up schlieren images of the Slow/N_2 reacting mixing layer (not shown), the wake of the splitter tip extends to about 3 mm downstream of the splitter tip, and distinct vortices shedding off the splitter tip can be discerned immediately downstream
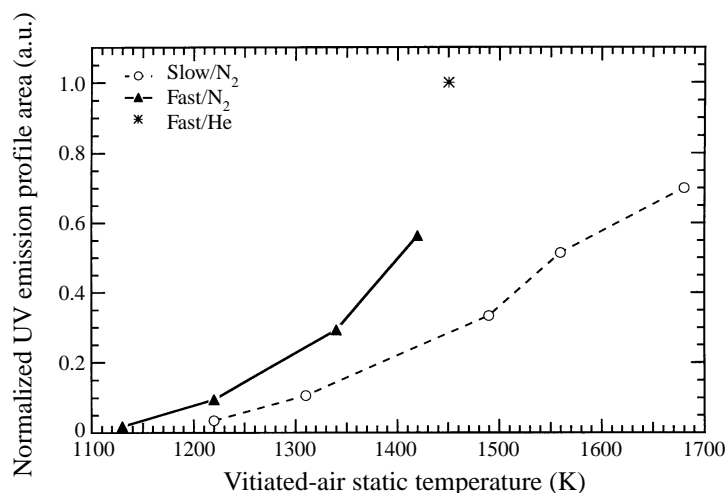
FIGURE 11. Area under UV emission signal profiles normalized by the local mixing layer thickness as a function of the vitiated-air-stream static temperature ($x = 22$ cm).

of this point. After about 5 cm, the mixing layer degenerates into a more indistinguishable structure. The ignition distances observed for the Slow/N_2 are generally less than 3 cm, and the UV emission signal reaches its plateau level by 8 cm. Thus, the influence of the wake region of the splitter tip on the ignition behaviour cannot be ignored.

5.3.2. *Signal strengths*

Side-view UV emission images acquired at the PLIF imaging station were analysed to compare the relative signal strengths over a range of vitiated-air-stream temperatures. As a measure of the integrated UV emission signal, signal profiles plotted as a function of transverse position were integrated and then normalized by the local mixing layer thickness. The normalized UV emission profile areas are plotted as a function of the vitiated-air-stream temperature in figure 11. The UV emission signals of the Fast/N_2 case are consistently higher than those of the Slow/N_2 case, suggesting it has a higher combustion intensity. The Fast/He case has the highest UV emission signals at the PLIF imaging conditions.

5.4. *Combined OH/acetone PLIF images*

5.4.1. *Instantaneous mixing layer structure*

A representative selection of combined OH/acetone PLIF side- and plan-view images of the reacting mixing layers acquired under the conditions listed in table 1 are shown in figures 12–17. In all of the images, the flow is from left to right, and the centre of the image is 22 cm downstream of the splitter tip. The side-view images are approximately 7.7 cm wide and 5 cm high (200×133 pixels), and the plan-view images are 7.7 cm wide and 4 cm high (200×95 pixels). The images have been corrected for background scattering, laser-sheet energy distribution and non-uniform camera response. In the plan views, the laser sheet was positioned above the centreline of the mixing layer so that the images would contain significant signal from both OH and acetone.

In the side-view images, the regions of maximum signal level at the bottom of the acetone images correspond to the low-speed free stream (fuel stream), and the regions of lower signal correspond to fluid from the fuel stream which has been entrained into
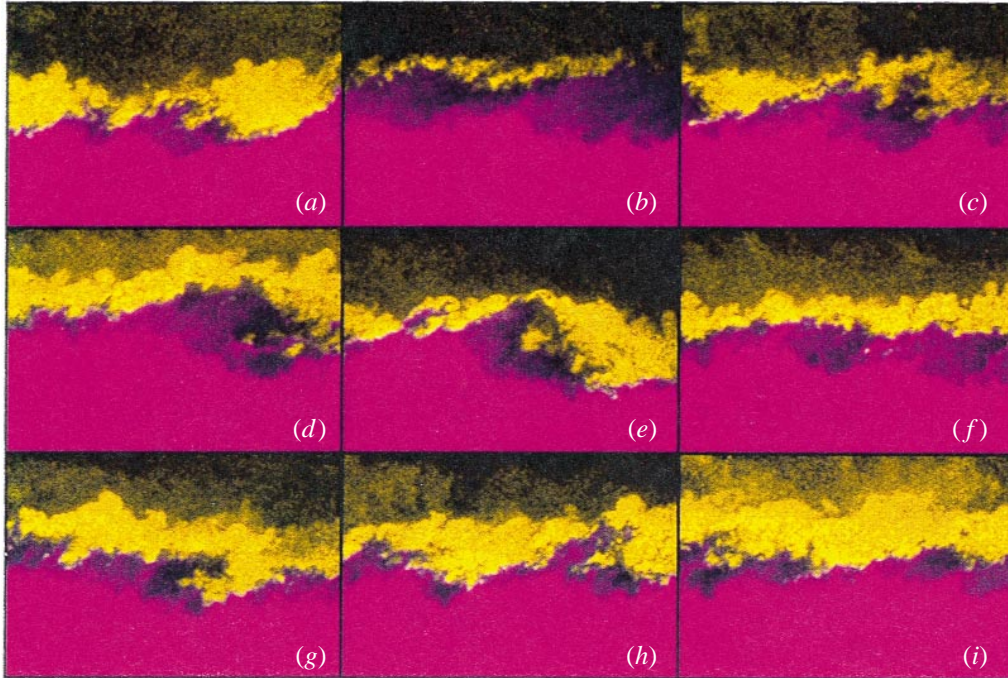
FIGURE 12. Single-pulse combined OH/acetone PLIF side-view images of the Slow/N_2 reacting mixing layer ($M_c = 0.32$; $r = 0.34$; $s = 5.4$). Flow is left to right; the vitiated-air stream is on top and the fuel stream is on the bottom. Each image is 7.7 cm wide and 5 cm high. The images are centred 22 cm downstream of the splitter tip.
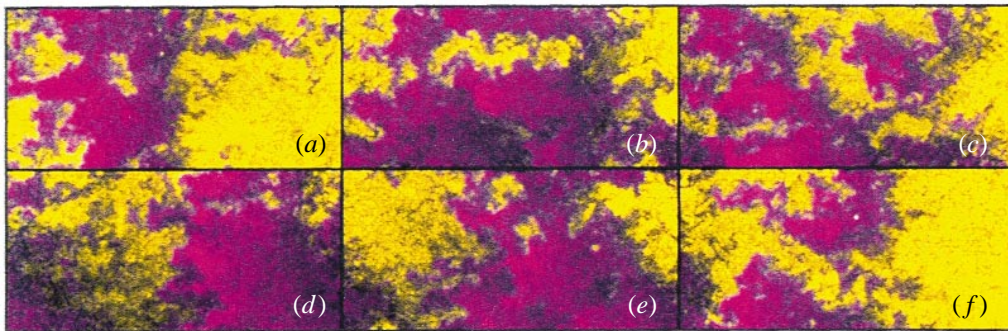
FIGURE 13. As figure 12 but plan-view images; the laser sheet is positioned at $y/\delta \approx 0.1$. Each image is 4 cm high.

the mixing layer and mixed (diluted) and possibly reacted with existing fluid in the mixing layer. Based on the analysis of the spectroscopy and chemistry of acetone presented in §4, the amount of unburned hydrogen at a point in the flow scales with the acetone signal at that point. Although acetone is not a conserved scalar, different signal levels necessarily indicate different mixture compositions; thus, higher acetone signals mark the cooler regions of the mixing layer rich in fuel-stream fluid, and lower acetone signals mark the hotter regions of the mixing layer rich in vitiated-air-stream fluid and combustion products.

High OH signal levels are found in the mixing layer primarily in regions adjacent to the vitiated-air stream with the instantaneous upper edge of the mixing layer coinciding
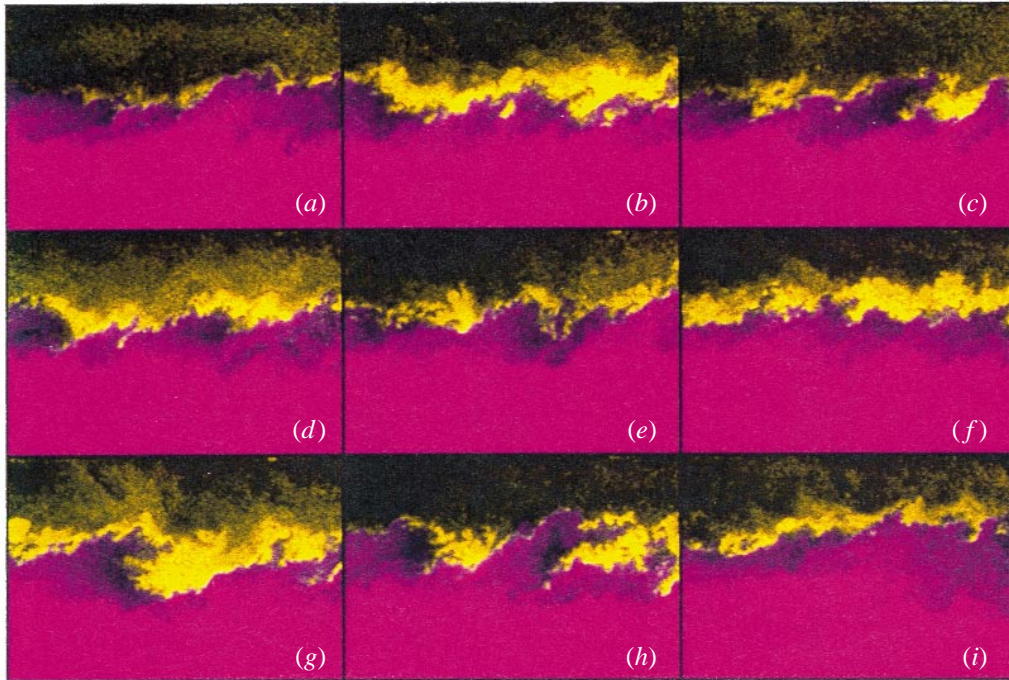
FIGURE 14. Single-pulse combined OH/acetone PLIF side-view images of the Fast/He reacting mixing layer ($M_c = 0.35$; $r = 0.37$; $s = 0.75$). Other details as figure 12.
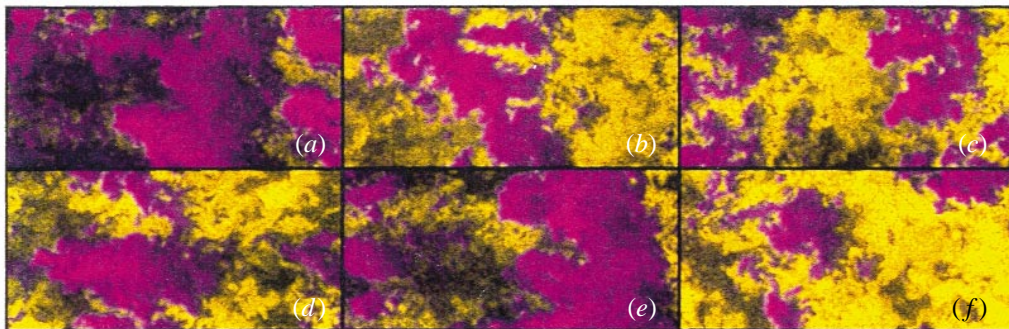
FIGURE 15. As figure 14 but plan-view images; the laser sheet is positioned at $y/\delta \approx 0.2$. Each image is 4 cm high.

with the upper edge of the regions of high OH signal. Residual OH from the vitiation heater is visible in the vitiated-air stream. Based on measurements of the imaging system sensitivity, the peak OH mole fraction in the reacting mixing layers is estimated to about 2000 p.p.m. The average OH mole fraction in the vitiated-air stream is about 300 p.p.m. The analysis of the OH fluorescence signal as a function of mixture fraction in the mixing layer presented in §4 indicates that the maximum error associated with assuming OH fluorescence signal is proportional to OH concentration is $\pm 10 \%$.

In the overlaid OH/acetone images, a distinct division is noticeable between the regions of high OH signal and high acetone signal; that is, high signal levels of OH and acetone are mutually exclusive. This observation is consistent with the notion that the probability of finding OH is highest in the hotter regions of the mixing layer which will necessarily be lean in fuel-stream fluid and therefore will have lower acetone signals.
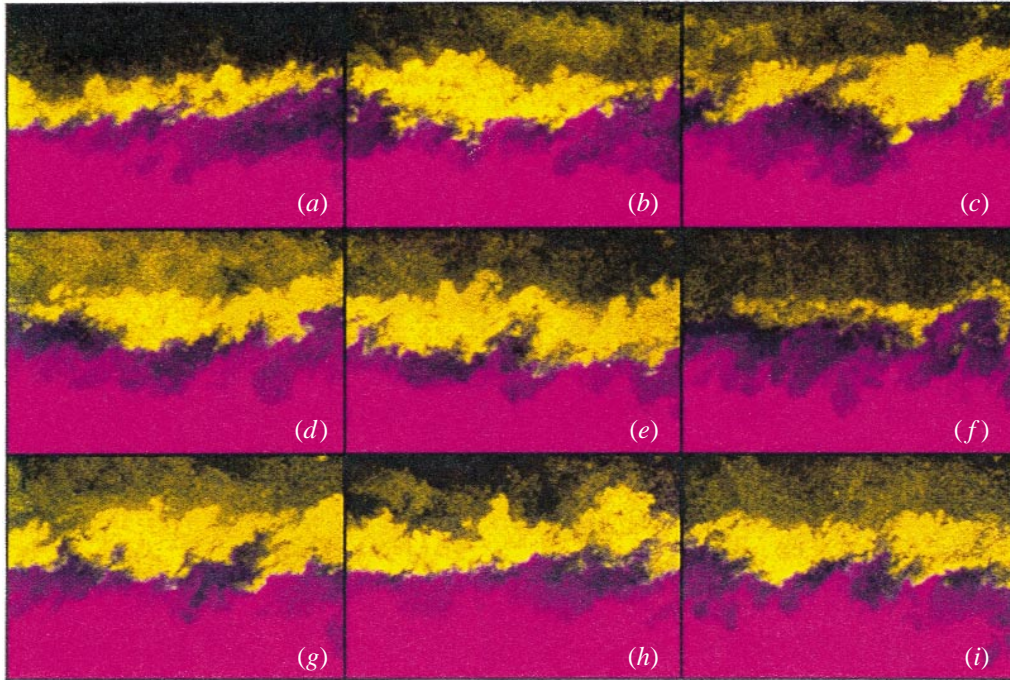
FIGURE 16. Single-pulse combined OH/acetone PLIF side-view images of the Fast/N₂ reacting mixing layer ($M_c = 0.70$; $r = 0.15$; $s = 5.1$). Other details as figure 12.
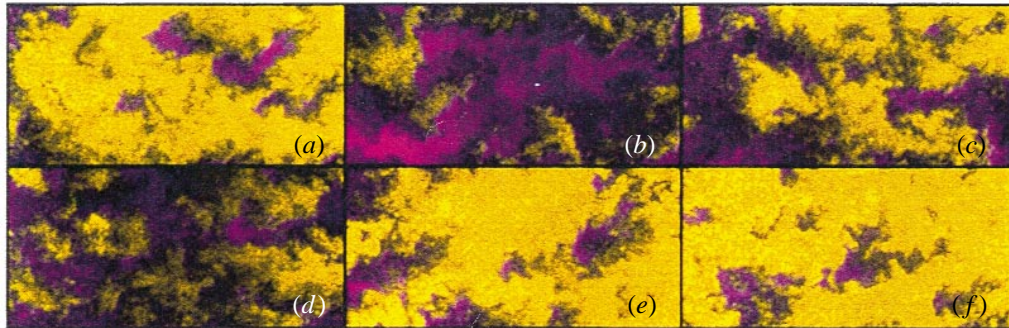
FIGURE 17. As figure 16 but plan-view images; the laser sheet is positioned at $y/\delta \approx 0.2$. Each image is 4 cm high.

Plots of single pixel rows and columns in the OH and acetone side-view images are shown in figures 18–20. These plots highlight features of the large-scale structure of the reacting mixing layers which will be discussed in detail in the following sections. The acetone fluorescence signals have been normalized by the average low-speed-stream value, and the OH signals have been normalized by the maximum instantaneous signal observed in all of the images acquired for all three cases. Based on the root-mean-squared noise levels, the peak signal-to-noise ratios of the acetone and OH images are approximately 12 and 10, respectively. Visible emission from the combustion zone in the mixing layer creates a small interference in the acetone images. Also, an interference is present in the OH images corresponding to acetone fluorescence from
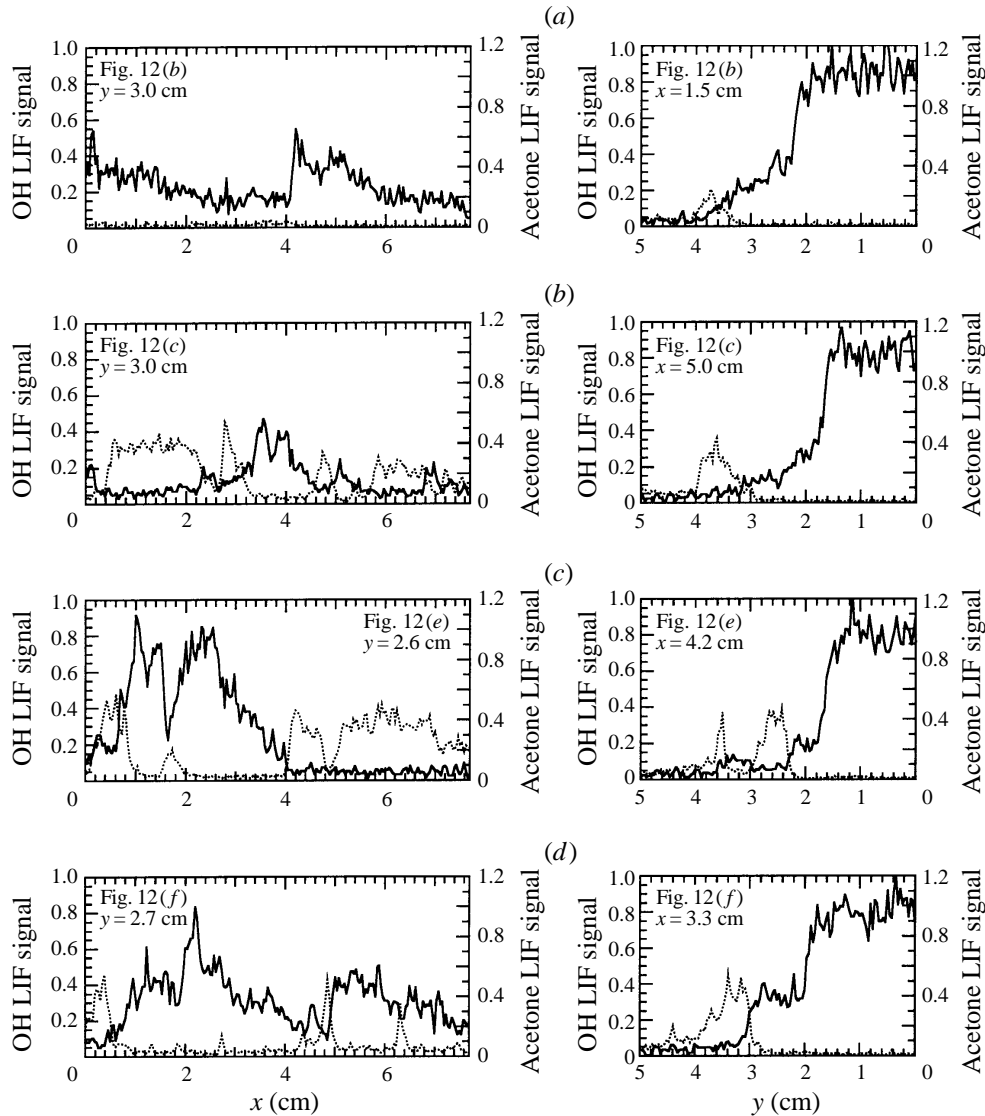
FIGURE 18. Plots of signal values from single pixel rows and columns of the single-pulse combined OH/acetone PLIF side-view images of the Slow/N$_2$ reacting mixing layer ($M_c = 0.32$; $r = 0.34$; $s = 5.4$): streamwise cut (left) and transverse cut (right). The dashed and solid lines are LIF signal of OH and acetone, respectively. The corresponding image and the location of the row and column plotted are indicated on each graph. The lower left-hand corner of the side-view images corresponds to $(x, y) = (0, 0)$.

the low-speed stream. These interferences, which are both due to incomplete rejection by the optical filtering, cannot be removed by a simple subtraction process since they are present only in a particular region of the flow, the domain of which varies from image to image; however, the sources of interference are generally separated from the regions of interest and therefore do not represent a major obstacle in the analysis of the images.
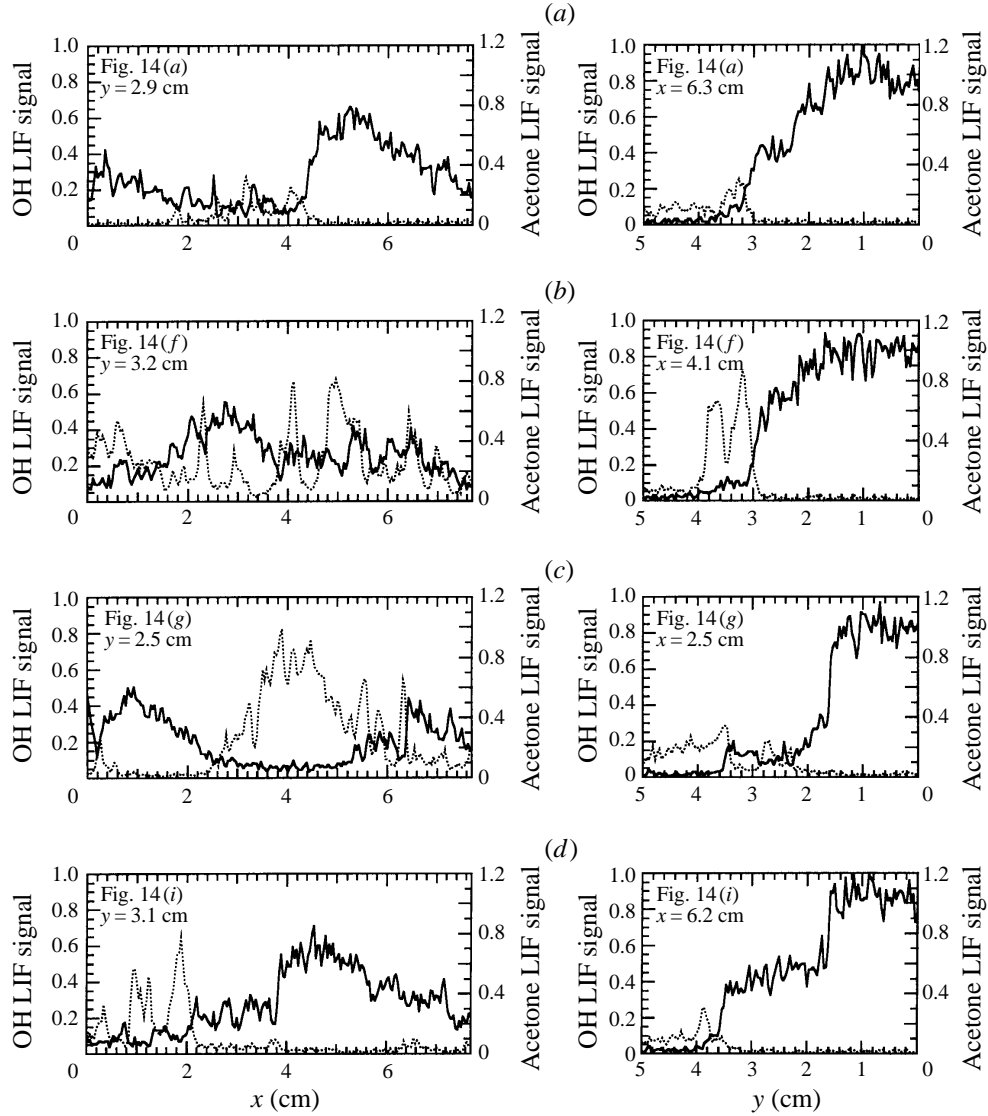
FIGURE 19. As figure 18 but for the Fast/He reacting mixing layer ($M_c = 0.35$; $r = 0.37$; $s = 0.75$).

Low-compressibility cases

In previous studies, the two-dimensional spanwise-oriented vortical structures common to incompressible mixing layers have been observed in low-compressibility mixing layers with high frequency. These structures generally occur in a periodic fashion, and large-scale penetration of pure high- and low-speed fluid into the mixing layer is observed. Ideally, these structures are modelled as entraining low-speed fluid from the upstream side and high-speed fluid from the downstream side; thus, their composition tends to be ramped predominately in the streamwise direction. In the present reacting mixing layers, therefore, the upstream side of these structures will be cool and fuel-rich while the downstream side of the structures will be hot and fuel-lean.

The side- and plan-view images of both low-compressibility cases, Slow/N_2 ($M_c =$
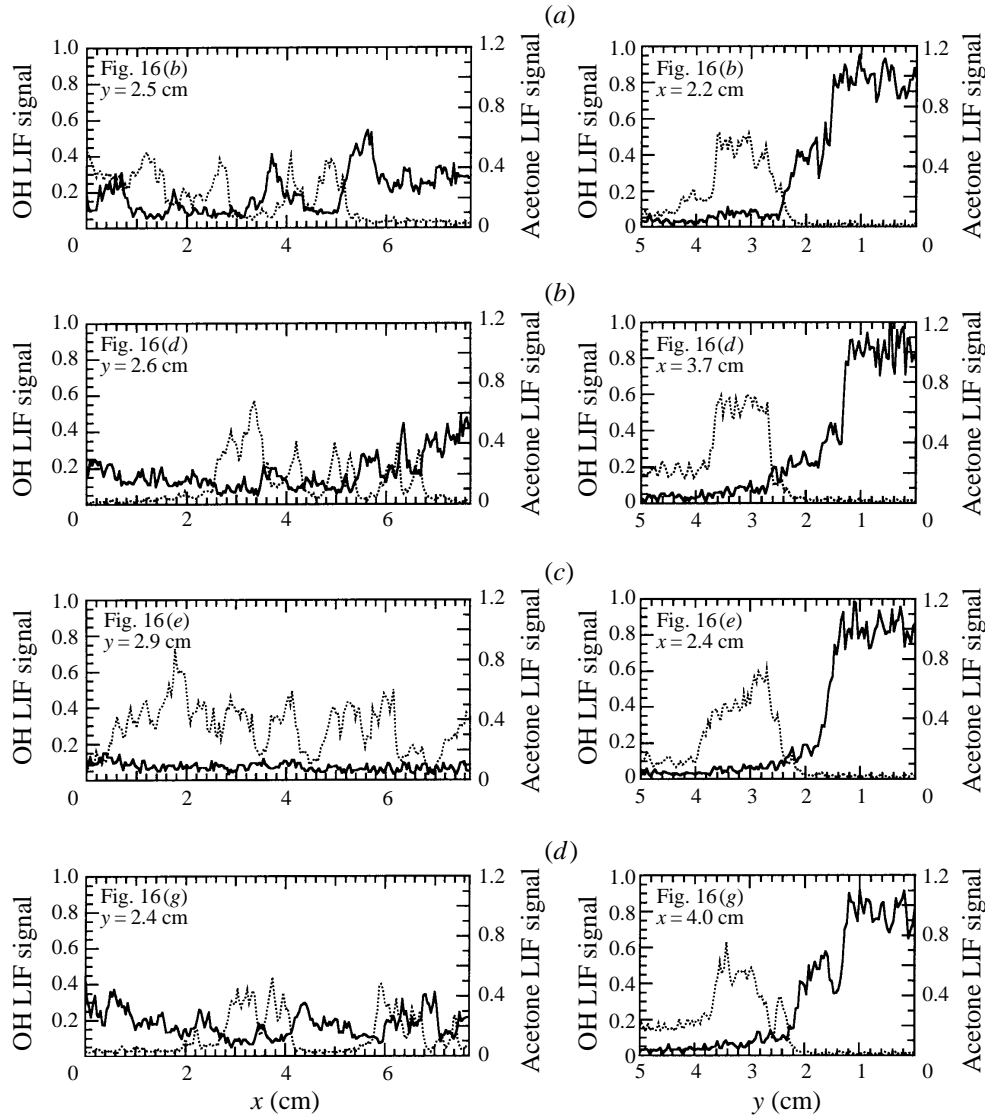
FIGURE 20. As figure 18 but for the Fast/N_2 reacting mixing layer ($M_c = 0.70$; $r = 0.15$; $s = 5.1$).

0.32) and Fast/He ($M_c = 0.35$), show structural features which are consistent with those outlined above. Several of the side-view images show roller-like structures (e.g. figure 12 c, d; figure 14 e, g) and significant penetration of low-speed fluid into the mixing layer. Streamwise ramping of the acetone signal across the structures is observed, and OH exists primarily on the top edges and front faces of the roller-like structures. Some of the cuts through the images also show that the acetone concentration is ramped in the streamwise direction yet is more uniform in the cross stream direction (e.g. figures 18 d and 19 d). On average, the acetone signals within the mixing layer are higher in the Fast/He case than in the Slow/N_2 case, and the regions of OH in the Fast/He mixing layer appear thinner and more localized. As will be discussed, these observations are consistent with the fact that the Fast/He case has a lower entrainment ratio.
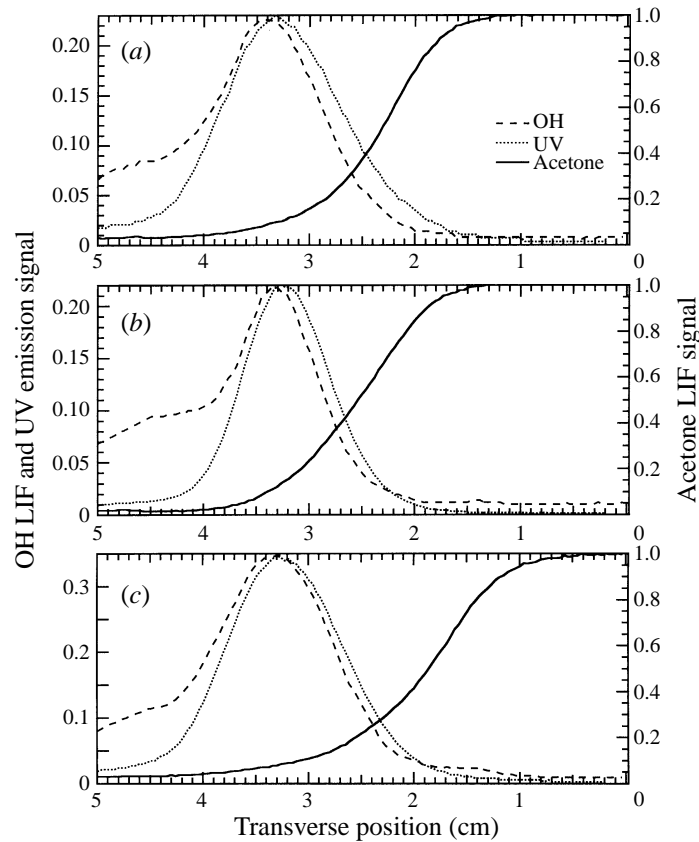
FIGURE 21. Averages of the OH and acetone LIF and UV emission signals as a function of transverse position in the reacting mixing layers: Slow/N_2 (*a*), Fast/He (*b*) and Fast/N_2 (*c*). The bottom of PLIF images corresponds to $y = 0$ cm.

The plan-view images of the low-compressibility mixing layers show spanwise-oriented bands of acetone and OH signal, consistent with a predominantly two-dimensional mixing layer structure. Streamwise ramping of the acetone signal is also seen in the plan-view images. The upstream side of the bands of acetone signal appear convoluted, a feature which reflects the presence of the streamwise-oriented smaller-scale vortices known to exist in incompressible mixing layers (e.g. Bernal & Roshko 1986; Clemens & Mungal 1995; Karasso & Mungal 1996).

High-compressibility case

Consistent with the non-reacting mixing layer experiments of Clemens & Mungal (1995), the side-view images of the Fast/N_2 case (figure 16) show that the mixing layer appears less organized with more irregular edges. Large penetrations of fluid from the low-speed stream are not observed as frequently, and OH appears in broad and contiguous regions. (The mixing layer thickness of the Fast/N_2 case is larger than that of the incompressible cases owing to its higher growth rate.) The cuts through the compressible mixing layer images (figure 20) indicate that streamwise ramping of the acetone signal is not as prevalent, and when streamwise ramping is observed, it does not appear to be associated with the type of organized motions seen in the low-compressibility mixing layers. Comparing the high- and low-compressibility plan-view
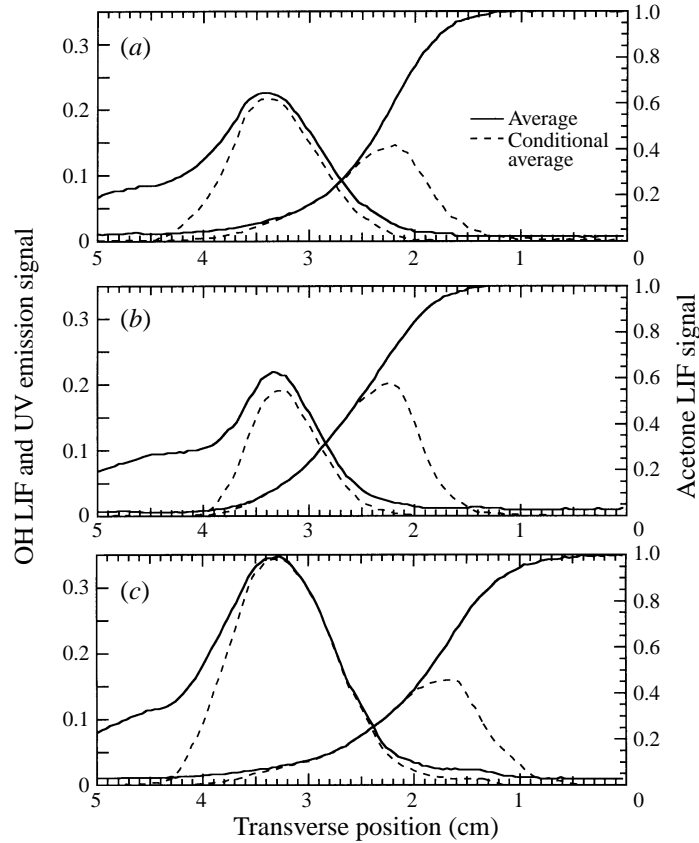
FIGURE 22. Averages and conditional averages of the OH and acetone LIF signals as a function of transverse position in the reacting mixing layers: Slow/N_2 (*a*), Fast/He (*b*) and Fast/N_2 (*c*). The bottom of the PLIF images corresponds to $y = 0$ cm.

images (figure 17), the banded structure of the Fast/He and Slow/N_2 cases is less evident in the Fast/N_2 case where obliquely and streamwise-oriented structures of OH and acetone dominate the images, indicating a more three-dimensional structure.

5.4.2. *Comparison of OH and acetone LIF signals*

The average OH and acetone LIF and UV emission signals for all three reacting mixing layers are plotted as a function of transverse position in figure 21. The fluorescence signal profiles were obtained by frame-averaging approximately 80 instantaneous OH and acetone PLIF images and subsequently averaging the centre 2 cm of the frame-averaged images. The UV emission profiles were obtained in a similar fashion. The acetone LIF signals are normalized by the low-speed stream value, and the OH LIF signals are normalized by the peak OH signal observed in all cases. The UV emission signals have been normalized such that the peak value of the profile is equal to that of the OH LIF profile. Since the UV emission is produced primarily by radical recombination reactions which scale nonlinearly with the local radical concentrations (e.g. Davis, McGregor & Mason 1973; Kaskan 1959), the ratio of the UV emission signal in the mixing layer to that in the vitiated-air stream is much higher than the corresponding OH LIF signal ratio. Additionally, the UV emission profile appears to be shifted toward the centre of the mixing layer, although one would not
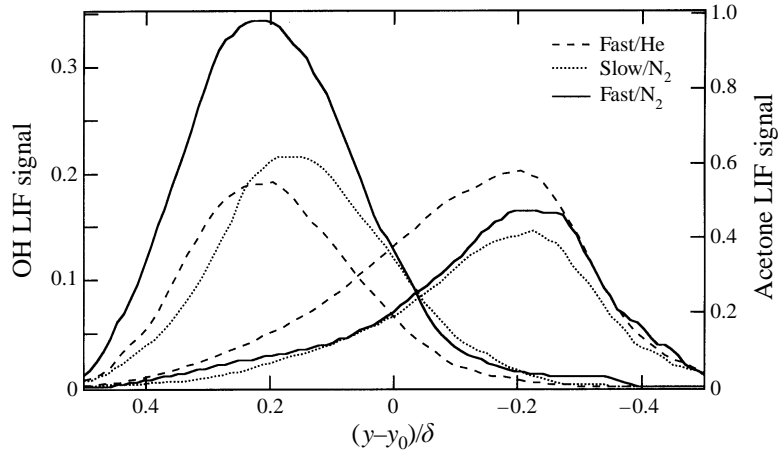
FIGURE 23. Comparison of conditionally-averaged OH and acetone LIF signals as a function of normalized transverse position $((y-y_0)/\delta)$ in the reacting mixing layers. Left-hand curves correspond to OH; right-hand curves correspond to acetone.

expect the OH LIF and UV emission profiles to be aligned since the regions of maximum radical recombination rates and maximum radical concentrations do not necessarily coincide.

The average OH and acetone fluorescence signals as a function of transverse position in the mixing layer along with profiles of conditionally averaged signals are shown in figure 22. The conditionally averaged profiles were calculated by masking (i.e. thresholding) the free streams in each of the instantaneous OH and acetone images prior to frame-averaging to select those pixels associated with mixed fluid in the mixing layer. For example, in the acetone images, pixels with values below the signal level in the low-speed free-stream region and above the background level of the vitiated-air stream were selected. Since the imaging spatial resolution is not sufficient to fully resolve all the scales of the flow, it is understood that when the conditionally averaged measurements are referred to as a measurement of the mixed fluid, these measurements contain the effects of spatial averaging.

At each point in the mixing layer, the difference between the conditionally averaged profiles and the average profiles indicates the degree to which pure free-stream fluid contributes to the average signal at that point. For the Fast/He and Slow/N_2 cases, the OH conditional averages are below the averages throughout the mixing layer, while those of the Fast/N_2 case show a much better correspondence. This difference between the high- and low-compressibility mixing layers is due primarily to the structural differences between the high- and low-compressibility mixing layers – the low-compressibility mixing layers have more intrusions of free-stream fluid into the mixing layer and therefore the contribution of the residual OH in the vitiated-air stream to the average signal in the mixing layer is greater.

Figure 23 is a comparison of the conditionally-averaged OH and acetone signals of the reacting mixing layers plotted in normalized transverse coordinates, where the transverse position in the mixing layer has been normalized by the mixing layer thickness. The position of the upper edge of the mixing layer is determined from the upper extent of the conditionally averaged OH signal curve; the conditionally averaged acetone signal curve is used similarly to determine the position of the bottom edge of the mixing layer. These plots allow a direct comparison of the OH and acetone distributions within the reacting mixing layers.
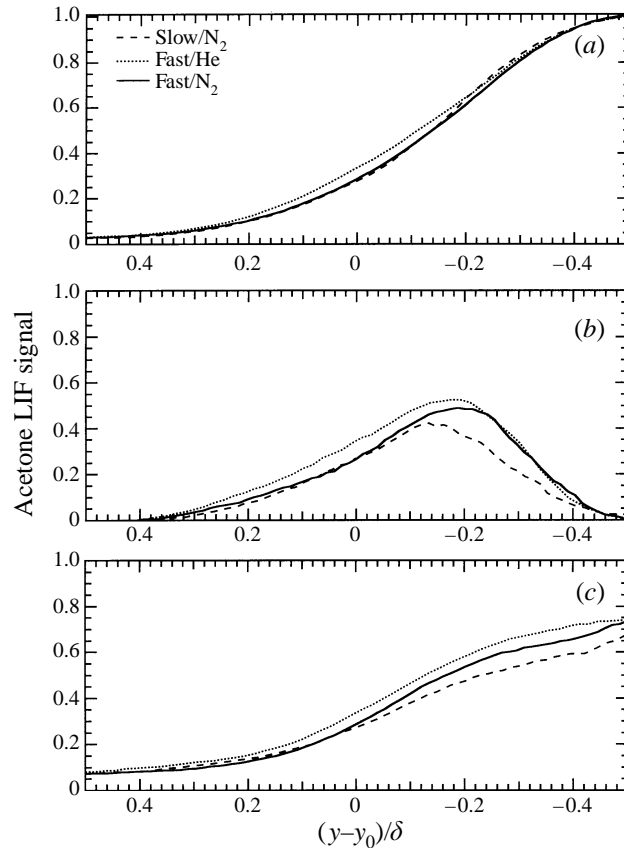
FIGURE 24. Averages and conditional averages of the acetone LIF signals as a function of normalized transverse position $((y-y_0)/\delta)$ in the non-reacting mixing layers: (*a*) averages, (*b*) conditional averages from masking process, and (*c*) conditional averages from histogram process.

Acetone signals

The conditionally averaged acetone signal profiles shown in figure 23 indicate that the Fast/He case has higher acetone signals within the mixing layer than the Slow/N_2 case, which is consistent with the fact that the Fast/He case, $(E_v)_i = 1.1$, has a higher relative rate of entrainment of fuel-stream fluid than the Slow/N_2 case, $(E_v)_i = 3.3$. Figure 23 also shows that the acetone signal levels of the Fast/N_2 case are intermediate to those of the Fast/He and Slow/N_2 cases, suggesting that it has an intermediate entrainment ratio. This result is not in agreement with the entrainment ratios derived using the incompressible mixing layer formula, which predicted $(E_v)_i = 3.8$ for the Fast/N_2 case – a value higher than the entrainment ratios of both the Fast/He and Slow/N_2 cases.

Since acetone is not a conserved scalar in the reacting mixing layers, its average signal level depends not only on the entrainment rate of acetone but also on the rate of consumption of acetone by the combustion. To investigate the trends observed in the reacting mixing layers, acetone PLIF images were acquired in non-reacting mixing layers having the same free-stream conditions as those listed in table 1, excluding the hydrogen in the fuel stream. The average and conditionally averaged acetone signals obtained in the non-reacting mixing layers are compared in figure 24 which shows two conditional averages: one obtained using a masking process and one obtained using a

histogram process. The masking process is the same one used to obtain the conditionally averaged OH and acetone signal profiles in figure 23. In the histogram process, each row of the non-reacting acetone images is histogrammed, and its mean value is determined; however, the range of signal values included in the averages excludes the free-stream signal levels. Thus, the histogram process also yields profiles of the mean acetone signal level of the mixed fluid in the mixing layer, except that it does not include the free-stream intermittency effects present in the masking process results. Comparison of the conditionally averaged acetone profiles in figures 23 and 24(*b*) shows very little change in the relative magnitude and distribution of acetone between the reacting and non-reacting mixing layers, suggesting that very little destruction of acetone by combustion is occurring.

Both sets of conditionally averaged acetone signal levels in the non-reacting mixing layers show the same trend as observed in the reacting mixing layers; that is, the Fast/N_2 case has average acetone signal levels intermediate to those of the Fast/He and Slow/N_2 cases, indicating that the compressible mixing layer (Fast/N_2) has an entrainment ratio lower than its incompressible counterpart (Slow/N_2). Consistent with these observations, Hall *et al.* (1991) measured a mean composition corresponding to $E_v \approx 1.0$ in a compressible mixing layer with free-stream conditions similar to those of the Fast/N_2 case, while the incompressible formula predicted $(E_v)_i = 4.5$ for those conditions. While the acetone measurements support the observations of Hall *et al.*, uncertainties in the acetone fluorescence measurements (i.e. spatial resolution, temperature dependence) prevent a conclusive assessment of the magnitude of the entrainment ratio shift.

OH signals

Based on the instantaneous OH PLIF images, comparable peak OH signals are observed in the Fast/N_2 and Slow/N_2 cases while significantly higher peak OH signals are observed in the Fast/He case. There are several factors which contribute to this difference. First, for a given mixture fraction and a given extent of reaction, the lower specific heat of helium compared to that of nitrogen results in higher temperatures in the mixing layer which can lead to higher OH production rates and therefore higher local OH concentrations. Secondly, compared to nitrogen, helium has a lower OH quenching cross-section; thus, for a given concentration of OH, higher OH LIF signals will be observed in the Fast/He case.

Comparing the conditionally averaged OH profiles of the low-compressibility mixing layers (figure 23), the peak of the conditionally averaged OH signal profile of the Fast/N_2 case is significantly higher than those of the Fast/He and Slow/N_2 cases. The difference between the peak heights of the two low-compressibility mixing layers is not significant considering the uncertainties in the OH LIF measurements. Since the Fast/N_2 and Fast/He cases share the same vitiated-air-stream conditions, differences between the two OH profiles can be directly attributed to differences in the mixing layers (e.g. compressibility or density ratio), keeping in mind the factors mentioned previously related to changing the fuel-stream diluent. While comparison of the Fast/N_2 and Slow/N_2 cases is complicated somewhat by uncertainty in the extent to which vitiated-air-stream radical concentration differences affect the OH levels in the mixing layers, experimental correlations made between the OH signals in the mixing layer and those in the vitiated-air stream indicate that the OH peak height difference between the Fast/N_2 and Slow/N_2 cases (50 %) is larger than these uncertainties (20 %) (Miller 1994).

Consistent with its lower entrainment ratio, the OH signal profile of the Fast/He
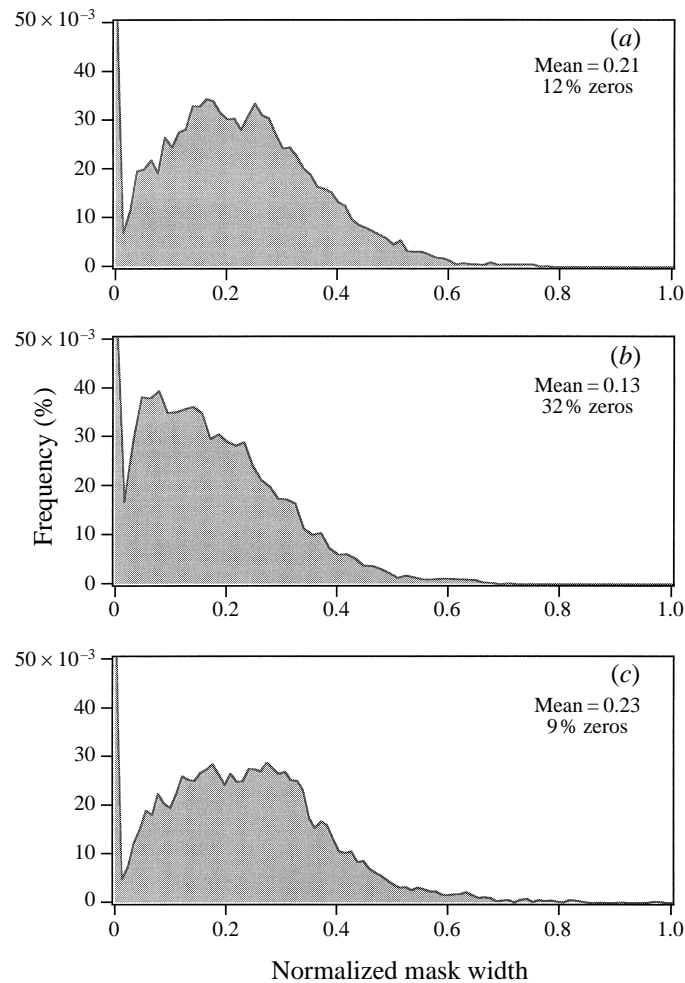
FIGURE 25. Histograms of the width of the OH regions in the OH PLIF side-view images of the reacting mixing layers: Slow/N_2 (*a*), Fast/He (*b*) and Fast/N_2 (*c*). Mask widths are normalized by the average widths of the mixing layers.

case peaks closer to the upper side of the mixing layer than does that of the Slow/N_2 case. Because the mean composition of the Fast/He mixing layer favours the fuel stream more (relative to the Slow/N_2 case), a smaller extent (spatial) of the mixing layer is able to initiate and support combustion. This is also apparent in the instantaneous OH PLIF images where the OH regions in the Fast/He case are generally thinner and more segmented. To illustrate these trends more clearly, histograms of the width of the OH regions expressed as a percentage of the average width of the mixing layer are plotted in figure 25. The width of the OH region is defined as the width of the mask used to select those pixels in the OH image having signal levels above that of the vitiated-air stream. Comparison of the OH width histograms shows that the regions of OH in the Fast/He case are about 40 % narrower than those in the Slow/N_2 case. Contributing to this lower average width is the higher frequency of observing a zero width, a factor which reflects the disconnected nature of the regions of OH in the Fast/He case.

Despite the differences in the instantaneous character of the regions of OH in the

mixing layers, the average OH profiles for the Fast/He and Slow/N_2 cases are surprisingly similar. Although the OH regions in the Fast/He case tend to be thinner and more localized, the higher instantaneous OH signals have a compensating effect. If the specific heat and fluorescence quenching differences between the two cases were taken into account, the average OH signal profile of the Fast/He case would be significantly lower than that of the Slow/N_2 case, a result which would be consistent with the notion that the lower entrainment ratio of the Fast/He case is detrimental to the combustion. The disconnected or patchy character of the regions of OH in the Fast/He case suggests that the streamwise vortices along the edges of the mixing layer (e.g. Bernal & Roshko 1986) play an important role in the combustion process. By preferentially entraining fluid from the vitiated-air stream, the streamwise vortices may provide localized regions in the mixing layer in which combustion can be initiated and sustained. Consistent with this hypothesis, the plan-view images of the Fast/He case (figure 15) have a greater tendency to show regions of OH which appear in streamwise streaks.

In the side-view OH/acetone PLIF images of the Fast/N_2 reacting mixing layer (figure 16), OH is generally present in broad and contiguous regions. The histograms of the OH widths (figure 25) show that the mean width of the regions of OH in the Fast/N_2 case is slightly larger than that of the Slow/N_2 case. Additionally, the average OH signals in the Fast/N_2 mixing layer are about 50% higher than those observed in both low-compressibility mixing layers. The acetone measurements presented above indicate that the Fast/N_2 mixing layer has an entrainment ratio lower than that of the Slow/N_2 case. In fact, the entrainment ratio measurement of Hall *et al.* (1991) suggests that the entrainment ratio of the Fast/N_2 case is quite close to that of the Fast/He case. Considering the observed effect of the entrainment ratio on the combustion in the low-compressibility mixing layers, one would expect that the regions of OH in the Fast/N_2 mixing layer would be narrower than those in the Slow/N_2 mixing layer; hence, the coexistence of broad regions of OH and high acetone signals in the compressible mixing is a surprising result.

5.4.3. *Comparison of OH LIF and UV emission signals*

For the conditions listed in table 1, the Fast/N_2 reacting mixing layer has UV emission signals higher than those in the Slow/N_2 mixing layer, supporting the trends of the OH LIF measurements. In fact, the UV emission signals of the Fast/N_2 case are consistently higher than those of the Slow/N_2 case over the entire range of temperatures investigated (figure 11). While the Fast/N_2 case has higher average OH LIF signals than the Fast/He case, its UV emission signals are lower. As mentioned earlier, because the UV emission from OH depends nonlinearly on the local radical concentrations, the relative magnitudes of the mean OH LIF and UV emission signals cannot be compared directly. Since the Fast/He reacting mixing layer has the higher peak OH signals in the instantaneous images, it is plausible that the nonlinear weighting of these signals is responsible for the higher UV emission signals. In fact, by scaling the signals in the instantaneous OH PLIF images using a power law consistent with OH emission measurements in laminar flames ($S_{UV} \propto [OH]^n$ where $n = 5$–7) and subsequently averaging the instantaneous images, this possibility has been confirmed (Miller 1994). Thus, the UV emission measurements support the conclusions drawn from the OH LIF measurements regarding the relative combustion intensity of the reacting mixing layers.

6. Discussion

Based on the combined OH/acetone PLIF and UV emission imaging results, compressibility primarily affects the reacting mixing layer in two ways. First, as indicated by the acetone measurements, the entrainment ratio of the compressible mixing layer is lower (i.e. closer to unity) than that of its low-compressibility counterpart. Secondly, the compressible mixing layer has slightly wider regions of OH and 50% higher average OH signals, which was unexpected considering that lowering the entrainment ratio decreased the average width of the regions of OH at low compressibilities.

To understand these observations, the effect of compressibility on scalar mixing must be considered in more detail. Several investigators have reported a decrease in the root-mean-square (RMS) turbulent fluctuations associated with the velocity (Goebel & Dutton 1991; Elliott & Samimy 1990) and scalar fields (Clemens & Mungal 1995; Clemens & Paul 1995), and there is evidence that the decrease is more pronounced on the high-speed side of the mixing layer (Clemens & Paul 1995; Bonnet *et al.* 1993). Using a cold-chemistry technique, which is insensitive to spatial resolution effects, to measure the amount of pure free-stream fluid in the mixing layer, both Clemens & Paul (1995) and Island (1997) have observed that the penetration of free-stream fluid into the mixing layer decreases with increasing compressibility. These results suggest that a more consistent molecularly mixed fluid composition, that is one which has smaller fluctuations about the mean, is observed at each transverse location in the mixing layer at higher compressibilities. This trend is also evident in the probability density functions (PDF) of the mixed-fluid composition derived from passive scalar measurements (Clemens & Mungal 1995; Clemens & Paul 1995). By combining the results of the passive scalar and cold chemistry measurement techniques, Island (1997) determined that the mean composition of the molecularly mixed fluid near the edges of the mixing layer becomes increasingly biased towards the composition of the adjacent free stream as compressibility increases, suggesting that the mixed-fluid composition PDF becomes more marching. Recent results of a DNS simulation of a temporally evolving annular mixing layer by Freund (1997) show that the PDF indeed changes from a non-marching to a marching character with increasing compressibility.

Using idealized models of the large-scale turbulent structures observed in the high- and low-compressibility mixing layers, Clemens & Mungal (1995) demonstrated the effect of the structural changes induced by compressibility on the PDF of mixed-fluid composition. The streamwise-ramped and cross-stream uniform structures observed primarily in the low-compressibility mixing layer produce a non-marching PDF, which has a preferred mixture fraction that is invariant with transverse location in the mixing layer, while the cross-stream-ramped structures observed primarily in the compressible mixing layer produce a marching PDF. Additionally, the PDF produced by the streamwise-ramped and cross-stream uniform structures is broader so that at each transverse position in the mixing layer, a larger range of mixture compositions is probable. Based on these models, the PDF of the high-compressibility mixing layer is expected to be more marching and narrower than that of the low-compressibility mixing layer, a result which is consistent with the experimental observations cited above.

The instantaneous flow structures observed in the high- and low-compressibility mixing layers do not always resemble the idealized models – occasionally cross-stream ramping is observed in the low-compressibility mixing layer and streamwise ramping is observed in the high-compressibility mixing layer. In fact, the PDFs reported for fully developed low-compressibility mixing layers are not non-marching; that is, no

preferred mixture fraction is evident (Batt 1977; Clemens & Mungal 1995; Clemens & Paul 1995; Karasso & Mungal 1992, 1996). Since these PDF results were derived from passive scalar measurements which did not fully resolve all of the spatial scales of the flows, care must be used in their interpretation. The chemically reacting results of Karasso & Mungal (1996), which were not sensitive to the spatial resolution effects, also indicate that the fully developed incompressible mixing layer PDF is not non-marching; however, their results indicate that the PDF is not completely marching either. Rather, Karasso & Mungal conclude that after a sufficient number of vortex pairings, the PDF evolves into a distribution intermediate to non-marching and marching, which they term 'tilted'. Although the incompressible mixing layer PDF is not purely non-marching, concepts such as the entrainment ratio, which is equivalent to the preferred mixture fraction, are still useful, as illustrated by the measurements of Frieler & Dimotakis (1988) who observed that an increase in the density ratio increases the mean mixture fraction at all points across the mixing layer.

The basic trends predicted using the idealized models of the turbulent structures are consistent with the experimental observations discussed above: compared to the low-compressibility mixing layer, a smaller range of mixed-fluid compositions is observed at a given position in the compressible mixing layer (narrower PDF), and the mean mixed-fluid composition favours that of the adjacent free stream near the edges of the compressible mixing layer (more marching PDF). Thus, although the streamwise-ramped cross-stream uniform structures do not completely dominate the low-compressibility mixing layer so that its PDF is purely non-marching, they still have a definite influence on the character of the PDF. As compressibility increases and the mixing layer becomes more three-dimensional, the classical two-dimensional structures are rarely observed and their influence on the PDF is diminished. These observations provide clear evidence of the effect of the structural changes induced by compressibility on the scalar field in the mixing layer and demonstrate that the idealized models of the mixing layer structures and their corresponding PDFs are useful for understanding the effect of compressibility on the scalar field.

Using the model PDFs discussed above, it is possible to rationalize the observations made in the present experiments. Figure 26 shows model PDFs for the three reacting mixing layer cases. The PDFs, which indicate the probability of finding a particular mixture composition at a given position in the mixing layer, are plotted in terms of the high-speed volumetric mixture fraction, $\xi_v = V_1/(V_1 + V_2)$. Pure low-speed fluid corresponds to $\xi_v = 0$, and pure high-speed fluid corresponds to $\xi_v = 1$. The streamwise-ramped and cross-stream uniform structures in the low-compressibility mixing layers, Fast/He ($M_c = 0.35$, $s = 0.75$) and Slow/N_2 ($M_c = 0.32$, $s = 5.4$), produce a non-marching PDF; thus, both model PDFs are idealized as being non-marching. Since the entrainment ratio of the Slow/N_2 mixing layer, owing to its higher free-stream density ratio, is higher than that of the Fast/He case, the preferred mixture fraction of the Slow/N_2 case is positioned closer to the axis corresponding to pure high-speed fluid ($\xi_v = 1$), as shown by Konrad (1976). In the case of a non-marching PDF, the average value of each PDF profile is the same; that is, the average mixture fraction is not a function of transverse position in the mixing layer. For example, the Fast/He case has $E_v \approx 1$ which corresponds to $\xi_v = 0.5$; thus, all of the probability density function profiles are centred at $\xi_v = 0.5$. The Slow/N_2 mixing layer has $E_v \approx 3$; correspondingly, its preferred mixture fraction is positioned at $\xi_v = 0.75$. A higher probability of values of ξ_v closer to unity (i.e. of mixture compositions rich in fluid from the vitiated-air stream) will favour the formation and existence of OH as well as lead to lower acetone signals in the mixing layer. This is precisely the trend observed in the
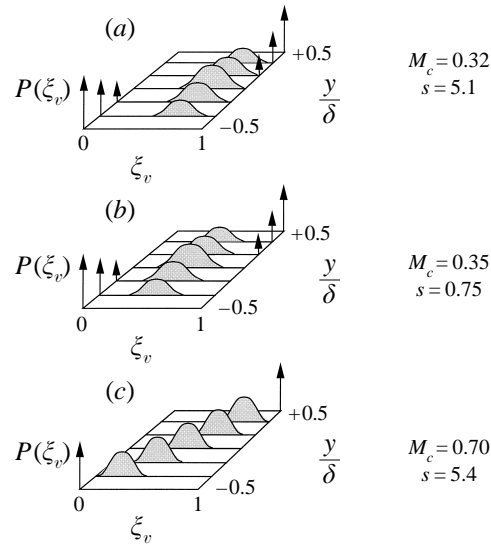
FIGURE 26. Model probability density functions for the reacting mixing layers: (*a*) Slow/N_2, (*b*) Fast/He and (*c*) Fast/N_2.

low-compressibility mixing layers: compared to the Fast/He case, the Slow/N_2 mixing layer has lower acetone signals and broader regions of OH.

The cross-stream-ramped structures of the compressible mixing layer produce a more marching PDF; thus, the model PDF of the Fast/N_2 case ($M_c = 0.70$, $s = 5.1$) in figure 26 is shown as marching. Since the purely marching PDF is symmetric about $\xi_v = 0.5$, the mean composition of the entire mixing layer is $\xi_v = 0.5$, corresponding to $E_v = 1$, a result which is consistent with the compressible mixing layer entrainment ratio measurements of Hall *et al.* (1991). Additionally, with the marching PDF, mixtures with values of ξ_v close to unity are probable in the upper regions of the mixing layer (i.e. $y/\delta > 0.5$). In terms of the present results, the Fast/N_2 reacting mixing layer, because of its more marching PDF, has an entrainment ratio lower than its incompressible counterpart (i.e. higher acetone signals), yet has regions in the upper portion of the mixing layer with compositions favouring that of the vitiated-air stream which lead to vigorous combustion (i.e. broad regions of OH). Thus, the changes in the scalar field associated with the large-scale structural changes induced by compressibility have a definite effect on combustion in the mixing layer, and the observed trends can be understood in terms of how the large-scale structural changes (2D → 3D) affect the PDF (non-marching → marching).

The more marching PDF of the compressible mixing layer is consistent with the increased role of smaller-scale motions in the entrainment process. Being of smaller scale, these motions would preferentially entrain free-stream fluid into the adjacent regions on each side of the mixing layer, leading to a more marching PDF. In fact, the model of compressible turbulence of Breidenthal (1992) suggests that as compressibility increases, the length scale over which communication between regions of the mixing layer can occur decreases. As the length scale of the largest turbulent motions decreases relative to the width of the mixing layer, the more applicable gradient diffusion models will become; thus, these types of mixing models may be appropriate for modelling turbulent transport in the compressible mixing layer. The combined influences of heat release and compressibility can have a dramatic effect on entrainment and combustion in the mixing layer, as evidenced by the direct numerical simulations of Planche (1992)

which predict that a 'co-layer' structure evolves with the upper and lower regions of mixing layer preferentially entraining fluid from the adjacent free streams but with only limited interaction between these two regions. This image of the mixing layer structure is reminiscent of the stratified nature of the OH and acetone regions in the compressible mixing layer PLIF visualizations (figure 16); however, based on the results of Planche, the heat release levels in these experiments are not sufficient to produce co-layers.

Based on the OH LIF and UV emission measurements, compressibility has a beneficial effect on combustion in the mixing layer, at least in this experimental configuration, which may be a result of the changes in the mixing field which accompany higher levels of compressibility discussed above. Perhaps, preferential entrainment by the streamwise motions in the compressible layer act to produce a hot fuel-lean region along the upper edge of the mixing layer which is conducive to OH formation. As indicated by the model PDFs, a narrower distribution of mixture compositions is expected at each position across the compressible mixing layer; thus, compared to the low-compressibility case, a more consistent mixture fraction may exist along the upper edge of the compressible reacting mixing layer which acts to enhance combustion.

Other mechanisms exist through which compressibility can affect combustion in the mixing layer. Since fuel and oxidizer must be molecularly mixed before chemical reaction can occur, the combustion will depend on the mixing efficiency of the mixing layer. Several measurements have been made of the effect of compressibility on mixing efficiency, indicating that for the range of convective Mach numbers considered in this work these effects are small (e.g. Clemens & Paul 1995; Island 1997). The Reynolds number can also affect the amount of molecularly mixed fluid in the mixing layer. Although Mungal, Hermanson & Dimotakis (1985) reported a decrease in the fraction of molecularly mixed fluid with increasing Reynolds number, more recent measurements by Island (1997) indicate that the changes in the mixing efficiency with Reynolds number are relatively weak. In fact, Island observed a slight *increase* in the amount of molecularly mixed fluid with increasing Reynolds number.

Since the large-scale structure of the mixing layer changes with increasing compressible, the strain-rate field, which can influence combustion, may also change. As discussed above, measurements of turbulent fluctuations (scalar and velocity) in compressibility mixing layers indicate that the fluctuations decrease with increasing compressibility, especially along the supersonic side of the mixing layer. The lower fluctuations may be a reflection of a decrease in the free-stream intermittency, but they may also be an indication of lower strain rates. Applying these observations to the present work, lower strain rates may exist along the top edge of the Fast/N_2 reacting mixing layer which act to enhance the combustion.

Temperature recovery due to the deceleration of entrained free-stream fluid can locally raise temperatures in the mixing layer and therefore enhance combustion. Im *et al.* (1994) have demonstrated computationally that, under certain conditions, the temperature rise produced by viscous dissipation can enhance ignition in laminar reacting mixing layers. In a turbulent mixing layer, entrained fluid can be decelerated by the pressure field as well as by viscous forces; thus, the conversion of kinetic energy to static enthalpy need not be associated only with the action of viscous dissipation. Using a simple scaling analysis in which all of the fluid in the mixing layer is assumed to be convecting at the average velocity of the two free streams (Miller 1994), a conservative estimate of the temperature recovery experienced by fluid entrained into mixing layers can be calculated. Based on the conditions listed in table 1, the temperature recoveries for the three reacting mixing layer cases are estimated to be:

Fast/N_2, 65 K; Slow/N_2, 15 k; and Fast/He, 5 K. While a temperature rise on the order of 100 K could be significant, it should be kept in mind that these estimates are conservative. Since all of the fluid in the mixing layer does not convect at the average free-stream velocity, the actual temperature recovery achieved in the mixing layer is likely to be only a fraction of the above estimate so that this effect is not considered significant in the present work.

7. Conclusions

The effect of compressibility on combustion in turbulent reacting mixing layers was investigated experimentally, with the free-stream density ratio and the convective Mach number being the principal parameters varied. Visualizations obtained using a combined OH/acetone planar laser-induced fluorescence imaging technique show that the reacting mixing layers have structural features consistent with those observed in non-reacting mixing layers at similar compressibilities, due in part to the modest level of heat release in these experiments. The primarily two-dimensional spanwise rollers common to incompressible mixing layers were observed in the low-compressibility ($M_c = 0.32, 0.35$) reacting mixing layers, and the distributions of OH and acetone within the mixing layers are consistent with idealized models of how these structures entrain free-stream fluid. The high-compressibility ($M_c = 0.70$) reacting mixing layer has a more disorganized and three-dimensional structure.

By varying the free-stream density ratio, the influence of the entrainment ratio on combustion in the low-compressibility mixing layers was investigated. Decreasing the density ratio from $\rho_2/\rho_1 = 5.4$ to 0.75 produced higher average acetone signals throughout the mixing layer and decreased the average width of the regions of OH. These observations are consistent with the fact that decreasing the density ratio increases the relative rate of entrainment of fluid from the fuel stream into the mixing layer.

Comparison of the average acetone signals in the mixing layers indicated that the high-compressibility case has an entrainment ratio lower than its incompressible counterpart. Despite this, the compressible mixing layer had wider OH widths and significantly higher OH signals, which is opposite to the trend observed in the low-compressibility mixing layers. The large-scale structural changes induced by compressibility are believed to be primarily responsible for the disparity between the behaviour of the high- and low-compressibility reacting mixing layers. It was shown that these observations can be reconciled by considering the effect of the structural changes (2D → 3D) on the probability density function of mixture composition in the mixing layer (non-marching → marching).

The average OH signals in the compressible mixing layer are about 50 % higher than those of its low-compressibility counterpart. Supporting this observation, time-averaged UV emission signals measured over a range of vitiated-air-stream temperatures were significantly higher as well. These results suggest that, at least for the present experimental configuration, compressibility has a beneficial effect on combustion in the mixing layer. The enhanced combustion in the compressible mixing layer may be attributed to changes in the entrainment process and the associated mixing field which accompany higher levels of compressibility.

REFERENCES

BARLOW, R. S., FOURGUETTE, D. C., MUNGAL, M. G. & DIBBLE, R. W. 1992 Experiments on the structure of an annular compressible reacting shear layer. *AIAA J.* **30**, 2244–2251.

BATT, R. G. 1977 Turbulent mixing of passive and chemically reacting species in a low-speed shear layer. *J. Fluid Mech.* **82**, 53–95.

BERNAL, L. P. & ROSHKO, A. 1986 Streamwise vortex structure in plane mixing layers. *J. Fluid Mech.* **170**, 490–525.

BOGDANOFF, D. W. 1983 Compressibility effects in turbulent shear layers. *AIAA J.* **21**, 926–927.

BONNET J. P., DEBISSCHOP, J. R. & CHAMBRES, O. 1993 Experimental studies of the turbulent structure of supersonic mixing layers. *AIAA Paper* 93-0217.

BRADSHAW, P. 1966 The effect of initial conditions on the development of a free shear layer. *J. Fluid Mech.* **26**, 225–236.

BREIDENTHAL, R. E. 1992 Sonic eddy – a model for compressible turbulence. *AIAA J.* **30**, 101–104.

BROADWELL, J. E. & BREIDENTHAL, R. E. 1982 A simple model of mixing and chemical reaction in a turbulent shear layer. *J. Fluid Mech.* **125**, 397–410.

BROWN, G. L. & ROSHKO, A. 1974 On density effects and large structure in turbulent mixing layers. *J. Fluid Mech.* **64**, 775–816.

BURROWS, M. C. & KURKOV, A. P. 1973 Analytical and experimental study of supersonic combustion of hydrogen in a vitiated airstream. *NASA TM*-X-2828.

CHENG, T. S., WEHRMEYER, J. A., PITZ, R. W., JARRETT, O. & NORTHAM, G. B. 1994 Raman measurement of mixing and finite-rate chemistry in a supersonic hydrogen-air diffusion flame. *Combust. Flame* **99**, 157–173.

CLEMENS, N. T. 1991 An experimental investigation of scalar mixing in supersonic turbulent shear layers. PhD thesis, Mechanical Engineering Department, Stanford University.

CLEMENS, N. T. & MUNGAL, M. G. 1992 Two- and three-dimensional effects in the supersonic mixing layer. *AIAA J.* **30**, 973–981.

CLEMENS, N. T. & MUNGAL, M. G. 1995 Large structure and entrainment in the supersonic mixing layer. *J. Fluid Mech.* **284**, 171–216.

CLEMENS, N. T. & PAUL, P. H. 1995 Scalar measurements in compressible axisymmetric mixing layers. *Phys. Fluids* A **7**, 1071–1081.

COHEN, L. S. & GUILE, R. N. 1969 Investigation of the mixing and combustion of turbulent, compressible free jets. *NASA CR*-1473.

CRAWFORD, M. E. & KAYS, W. M. 1976 STAN5 – A program for numerical computation of two-dimensional internal and external boundary layer flows. *NASA CR*-2742.

DAVIS, M. G., MCGREGOR, W. K. & MASON, A. A. 1973 OH chemiluminescent radiation from lean hydrogen-oxygen flames. *J. Chem. Phys.* **61**, 1352–1356.

DIMOTAKIS, P. E. 1986 Two-dimensional shear-layer entrainment. *AIAA J.* **24**, 1791–1796.

DIMOTAKIS, P. E. & LEONARD, A. 1994 Chemical reactions in turbulent mixing flows. *GALCIT Rep.* 94-3. California Institute of Technology, Pasadena, CA.

DUTTON, J. C., BURR, R. F., GOEBEL, S. G. & MESSERSMITH, N. L. 1990 Compressibility and mixing in turbulent free shear layers. *12th Symp. on Turbulence*, *Rolla*, *MO* p. A21-1.

ELLIOTT, G. S. & SAMIMY, M. 1990 Compressibility effects in free shear layers. *Phys. Fluids* A **2**, 1231–1240.

ELLIOTT, G. S., SAMIMY, M. & ARNETTE, S. A. 1992 Study of compressible mixing layers using filtered Rayleigh scattering based visualizations. *AIAA J.* **30**, 2567–2569.

ERDOS, J., TAMAGNO, J., BAKOS, R. & TRUCCO, R. 1992 Experiments on shear layer mixing at hypervelocity conditions. *AIAA Paper* 92-0628.

FREUND, J. B. 1997 Compressibility effects in a turbulent annular mixing layer. PhD thesis, Mechanical Engineering Department, Stanford University.

FRIELER, C. E. & DIMOTAKIS 1988 Mixing and reaction at low heat release in the non-homogeneous shear layer. *AIAA Paper* 88-3626.

GOEBEL, S. G. & DUTTON, J. C. 1991 Experimental study of compressible turbulent mixing layers. *AIAA J.* **39**, 538–546.

GRISCH, F., THURBER, M. C. & HANSON, R. K. 1995 Acetone fluorescence for temperature measurement. *Paper* 95F-192. Presented at *The Fall Meeting of the Western States Section*. The Combustion Institute.

GROSSMAN, F. 1993 Lazerinduzierte Fluoreszenz–Untersuchungen an 3-Pentanon, Aceton und Acetaldehyd. Diplomarbiet, Physikalisch-Chemisches Institut, Uni Heidelberg.

HALL, J. L., DIMOTAKIS, P. E. & ROSEMANN, H. 1991 Some measurements of molecular mixing in compressible turbulent shear layers. *AIAA Paper* 91-1719.

HALL, J. L., DIMOTAKIS, P. E. & ROSEMANN, H. 1993 Measurements in nonreacting compressible shear layers. *AIAA J.* **31**, 2247–2254.

HERMANSON, J. C. & DIMOTAKIS, P. E. 1989 Effects of heat release in a turbulent, reacting shear layer. *J. Fluid Mech.* **199**, 333–375.

HUANG, L.-S. & HO, C.-M. 1990 Small scale transition in a plane mixing layer. *J. Fluid Mech.* **210**, 475–500.

ISLAND, T. C. 1997 Quantitative scalar measurements and mixing enhancements in compressible shear layers. PhD thesis, Mechanical Engineering Department, Stanford University.

IM, H. G., CHEN, B. H., BECHTOLD, J. K. & LAW, C. K. 1994 Analysis of thermal ignition in the supersonic mixing layer. *AIAA J.* **32**, p. 341.

JACKSON, T. L. & GROSCH, C. E. 1989 Inviscid spatial stability of a compressible mixing layer. *J. Fluid Mech.* **208**, 609–637.

KARASSO, P. S. & MUNGAL, M. G. 1992 LIF measurements of mixing in turbulent shear layers. *6th Intl Symp. on Applications of Laser Techniques to Fluid Mechanics, Lisbon, Portugal*.

KARASSO, P. S. & MUNGAL, M. G. 1996 Scalar mixing and reaction in plane liquid shear layers. *J. Fluid Mech.* **323**, 23–63.

KASKAN, W. E. 1959 Abnormal excitation of OH in $H_2/O_2/N_2$ flames. *J. Chem. Phys.* **31**, 944–956.

KONRAD, J. H. 1976 An experimental investigation of mixing in two-dimensional turbulent shear flows with applications to diffusion-limited chemical reactions. PhD thesis, Graduate Aeronautics Laboratory, California Institute of Technology (available as *SQUID Tech. Rep.* CIT-8-PU).

LOZANO, A., YIP, B. & HANSON, R. K. 1992 Acetone: a tracer for concentration measurements in gaseous flows by planar laser-induced fluorescence. *Exps. Fluids* **13**, 369–376.

MASLOWE, S. A. & KELLY, R. E. 1971 Inviscid instability of an unbounded heterogeneous shear layer. *J. Fluid Mech.* **48**, 405–415.

MASUTANI, S. M. & BOWMAN, C. T. 1986 The structure of a chemically reacting plane mixing layer. *J. Fluid Mech.* **172**, 93–126.

MESSERSMITH, N. L., DUTTON, J. C. & KRIER, H. 1991 An experimental investigation of large scale structures in compressible mixing layers. *AIAA Paper* 91-0244.

MILLER, M. F. 1994 An experimental investigation of the effect of compressibility on combustion in a turbulent reacting mixing layer. PhD thesis, Mechanical Engineering Department, Stanford University.

MILLER, M. F., BOWMAN, C. T., MILLER, J. A. & KEE, R. J. 1989 A model for chemical reaction in a compressible, reacting mixing layer. *Paper* 89-110, presented at *The Fall Meeting of the Western States Section*. The Combustion Institute.

MILLER, M. F., ISLAND, T. C., SEITZMAN, J. M., BOWMAN, C. T., MUNGAL, M. G. & HANSON, R. K. 1994 An experimental investigation of supersonic reacting mixing layers. *AIAA Paper* 94-0823.

MILLER, M. F., ISLAND, T. C., YIP, B., BOWMAN, C. T., MUNGAL, M. G. & HANSON, R. K. 1993 An experimental study of the structure of a compressible, reacting mixing layer. *AIAA Paper* 93-0540.

MUNGAL, M. G. & DIMOTAKIS, P. E. 1984 Mixing and combustion with low heat release in a turbulent shear layer. *J. Fluid Mech.* **148**, 349–382.

MUNGAL, M. G. & FRIELER, C. E. 1988 The effects of Damköhler number in a turbulent shear layer. *Combust Flame* **71**, 23–34.

MUNGAL, M. G., HERMANSON, J. C. & DIMOTAKIS, P. E. 1985 Reynolds number effects on mixing and combustion in a reacting mixing layer. *AIAA J.* **23**, 1418–1423.

PAPAMOSCHOU, D. & ROSHKO, A. 1988 The compressible turbulent shear layer: an experimental study. *J. Fluid Mech.* **197**, 453–477.

PLANCHE, O. P. 1992 A numerical investigation of the compressible reacting mixing layer. PhD thesis, Mechanical Engineering Department, Stanford University.

RAGAB, S. A. & WU, J. L. 1989 Linear instabilities in two-dimensional compressible mixing layers. *Phys. Fluids* A **1**, 957–966.

SANDHAM, N. D. 1989 A numerical investigation of the compressible mixing layer. PhD thesis, Mechanical Engineering Department, Stanford University.

SANDHAM, N. D. & REYNOLDS, W. C. 1991 Three-dimensional simulations of large eddies in the compressible mixing layer. *J. Fluid Mech.* **224**, 133–158.

SARKAR, S. 1995 The stabilizing effect of compressibility in turbulent shear flow. *J. Fluid Mech.* **282**, 163–186.

SHIN, D. S. 1992 Stability of the compressible reacting mixing layer. PhD thesis, Mechanical Engineering Department, Stanford University.

TAIT, N. P. & GREENHALGH, D. A. 1992 2D laser-induced fluorescence imaging of parent fuel fraction in nonpremixed combustion. *Twenty-fourth Symp. (Intl) on Combustion*, pp. 1621–1628. The Combustion Institute.

WOLFF, D., SCHLÜTER, H., BEUSHAUSEN, V. & ANDRESEN, P. 1993 Quantitative determination of fuel air distributions in an internal combustion engine using PLIF of acetone. *Ber. Bunsenges. Phys. Chem.* **97**, 1738–1741.

YIP, B., MILLER, M. F., LOZANO, A. & HANSON, R. K. 1994 A combined OH/acetone planar laser-induced fluorescence technique for visualizing combusting flows. *Exps. Fluids* **17**, 330–336.